Modelling high-frequency seismograms at ocean bottom seismometers: effects of heterogeneous structures on source parameter estimation for small offshore earthquakes and shallow low-frequency tremors

Authors

Shunsuke TAKEMURA[1*], Suguru YABE[2], Kentaro EMOTO[3]

[1]Earthquake Research Institute, the University of Tokyo, 1-1-1 Yayoi, Bunkyo-ku, Tokyo 113-0032, Japan

[2]Geological Survey of Japan, National Institute of Advanced Industrial Science and Technology, Tsukuba Central 7, 1-1-1 Higashi, Tsukuba, Ibaraki 305-8567, Japan

[3]Geophysics, Graduate School of Science, Tohoku University, 6-3, Aramaki-aza-aoba, Aoba-ku, Sendai 980-8578, Japan

Running Title

Modelling HF seismograms at OBSs

Corresponding Author

Shunsuke Takemura

E-mail: shunsuke@eri.u-tokyo.ac.jp

Phone: +81 3-5841-5689

Summary

The source characteristics of offshore seismic events, especially regular (or fast) and slow earthquakes, can provide key information on their source physics and frictional conditions at the plate boundary. Due to strong three-dimensional heterogeneities in offshore regions, such as those relating to seawater, accretionary prism, and small-scale velocity heterogeneity, conventional methods using a one-dimensional Earth model may misestimate source parameters such as the duration and radiation energy. Estimations could become severe inaccuracies for small offshore seismic events because high-frequency (> 1 Hz) seismograms, which are strongly affected by three-dimensional heterogeneities, are only available for analysis because of their signal-to-noise ratio. To investigate the effects of offshore heterogeneities on source parameter estimation for small seismic events, we analysed both observed and simulated high-frequency seismograms southeast off the Kii Peninsula, Japan, in the Nankai subduction zone. Numerical simulations of seismic wave propagation using a three-dimensional velocity structure model clarified the effects of each heterogeneity. Comparisons between observations and model simulations demonstrated that the thick low-velocity accretionary prism has significant effects on high-frequency seismic wave propagation. Especially for shallow low-frequency tremors occurring at depths just below the accretionary prism toe, seismogram durations are significantly broader than an assumed source duration, even for stations with epicentral distances of approximately 10 km. Spindle-shape seismogram envelopes were observed even at such close stations. Our results suggest that incorporating three-dimensional heterogeneities is necessary for practical estimation of source parameters for small offshore events.

Keywords:

Computational seismology, earthquake ground motions, earthquake source observations, seismicity and tectonics, wave propagation, wave scattering and diffraction

1. Introduction

To understand the physics and characteristics of earthquake sources, seismologists analyse observed seismograms around the world. Following the correction of the frequency responses of seismometers and local site effects at each station, the observed seismograms provide information on the source rupture complexity and heterogeneous structures along each propagation path. For centroid moment tensor (CMT) inversion for teleseismic events or local crustal earthquakes using low-frequency (< 0.1 Hz) seismograms, path effects are typically evaluated by assuming a simple one-dimensional (1D) Earth model (e.g., Ekström et al., 2012; Kanamori & Rivera, 2008; Nakano et al., 2008) because low-frequency seismic waves are usually considered insensitive to structural heterogeneities. Given the recent developments in computer resources and three-dimensional (3D) subsurface structure models, CMT inversions using 3D velocity models have been practically conducted for not only crustal, but also offshore earthquakes (e.g., Hejrani et al. 2017; Takemura, Okuwaki, et al. 2020; Wang & Zhan 2020). The 3D heterogeneities in the offshore regions, such as seawater, accretionary prism, and small-scale velocity heterogeneity, are developed just beneath the epicentre regions of offshore subduction zone earthquakes. Thus, the 3D CMT method better constrains earthquake source characteristics compared to the 1D method, especially for offshore earthquakes.

Moment tensor inversion is only applicable to moderate-to-large earthquakes because of the signal-to-noise ratios of coherent low-frequency seismic signals. Thus, small events, such as microearthquakes or tectonic and volcanic tremors, are usually evaluated via methods based on the amplitudes or energies of high-frequency (> 1 Hz) seismic waves (e.g., Fletcher & McGarr, 2011; Gusev & Pavlov, 1991; Maeda & Obara, 2009; Nakahara, 2008; Poiata et al., 2018; Sawazaki & Enescu, 2014; Staudenmaier et al., 2016). The precise evaluation of small events is important for not only understanding source physics (e.g., Ellsworth & Bulut, 2018; Gomberg et al., 2016; Hawthorne et al., 2019; Ide et al., 2003; Supino et al., 2020; Thomas et al., 2016; Uchide & Ide, 2010), but also for monitoring crustal and volcanic activities (e.g., Battaglia & Aki, 2003; Kato et al., 2012; Kumagai et al., 2013; Kurokawa et al., 2016; Peng & Zhao, 2009; Yabe & Ide, 2014). The characteristics of high-frequency seismic waves, and related small-scale structural properties in onshore regions, have been widely investigated by numerical, theoretical, and observational approaches (e.g., Carcolé & Sato 2010; Chaput et al. 2015; Margerin 2005; Morioka et al. 2017; Saito et al. 2002; Takahashi et al. 2009; Takemura et al. 2016, 2017; Wegler et al. 2006). Consequently, the

estimated location and energy for onshore small seismic events are generally robust even with 1D conventional methods.

Due to long distances between onshore stations and offshore seismic sources, the source parameters of small offshore seismic events cannot be precisely determined from onshore seismic stations. Thus, temporal observations of ocean bottom seismometers (OBSs) have been extensively carried out. Around the Japanese Islands, permanent OBS networks of DONET and S-net (National Research Institute for Earth Science and Disaster Resilience, 2019c, 2019a) have been recently deployed. Several studies have used temporal OBS data or such permanent networks to estimate the source characteristics of small earthquakes and shallow low-frequency tremors (LFTs) (e.g., Nakano et al., 2015, 2019; Nishikawa et al., 2019; Tamaribuchi et al., 2019; Tanaka et al., 2019; Yabe et al., 2019). Offshore 3D heterogeneities, seawater, and bathymetry significantly affect seismic wave propagation even for low-frequency ground motions (e.g., Gomberg 2018; Guo et al. 2016; Nakamura et al. 2015; Shapiro et al. 1998, Takemura, Kubo, et al. 2019; Volk et al. 2017), complicated seismic waves such as T phase, Scholte, acoustic-coupled, and ocean-mode Rayleigh waves, as has been observed in previous studies (e.g., Haney & Tsai, 2017; Muyzert, 2007; Noguchi et al., 2016; Obara & Maeda, 2009; Okal, 2008; Takeo et al., 2014; Tonegawa, Fukao, Takahashi, et al., 2015). However, despite such complexities, 1D velocity structure models have been widely used in seismic source analyses, where incorrect estimations of source parameters may have been provided, especially for the duration and source energy.

Figure 1 shows examples of NS-component filtered velocity seismograms of onshore F-net and offshore DONET stations (National Research Institute for Earth Science and Disaster Resilience, 2019b, 2019a). The sensor orientations of X and Y at the DONET station (M.KMD14) were rotated to North (NS) and East (EW) by using estimations of sensor orientations of Nakano et al. (2012). The estimated event sizes of regular earthquakes in Figure 1 were similar. The event size of a shallow LFT, estimated by using an accompanied shallow very low-frequency earthquake (VLFE), was also similar. However, the observed waveforms of these events were very different. Although an F-net seismogram of an onshore regular earthquake showed a short-duration pulse-like *S*-wave envelope, a DONET seismogram of an offshore regular earthquake was broadened as result of the multiple wave packets. The seismogram of a shallow LFT was more complex, in which a spindle-shaped seismogram envelope was detected. In order to understand the differences in source processes among these seismic events, it is necessary to evaluate the effects of seismic wave

propagation through 3D strong heterogeneities in offshore regions, including the seawater, low-velocity accretionary prism, and small-scale velocity heterogeneity.

In this study, to investigate the effects of offshore heterogeneities on high-frequency seismic waves and source parameter estimations, we analysed simulated and observed high-frequency seismograms at offshore seismic stations. Using a realistic 3D offshore heterogeneous model, we conducted 3D numerical simulations of seismic wave propagation via open-source finite-difference method (FDM) software (OpenSWPC; Maeda et al., 2017). Simulated seismograms enable analysis of the effects of each heterogeneity on offshore high-frequency seismograms. By combining various structural model simulations and observed seismograms, we can evaluate the effects of the seawater, accretionary prism, and small-scale velocity heterogeneity on high-frequency seismograms at offshore stations. We also estimated a source time function (STF) of a shallow LFT via the conventional method, and conducted a numerical simulation of seismic wave propagation by using the estimated STF. By comparing simulated and observed seismogram envelope shapes, we also discuss reliable settings for source parameter estimations of offshore small seismic events via conventional methods.

2. Data and methods

The target region, southeast off the Kii Peninsula, southwest Japan (Figures 1 and 2a), has repeatedly experienced large megathrust earthquakes (e.g., Ando, 1975). To understand stress and frictional conditions of the megathrust zone along the Nankai Trough, regular and slow earthquakes around this region have been monitored by DONET stations (locations represented by diamond symbols in Figures 1 and 2a), operated jointly by the Japan Agency for Marine-Earth Science and Technology (JAMSTEC) and the National Research Institute for Earth Science and Disaster Resilience (NIED). Various small seismic phenomena, including small interplate and intraplate regular earthquakes and shallow slow earthquakes, have been observed by broadband seismometers installed at each DONET station. Interplate earthquake activity is quite low, except for activity of the 2016 southeast off Kii Peninsula earthquake (Nakano, Hyodo, et al., 2018; Wallace et al., 2016), but shallow slow earthquakes are often observed (e.g., Annoura et al., 2017; Araki et al., 2017; Nakano, Hori, et al., 2018; Toh et al., 2018). Precise source parameter estimation of such small phenomena is an important issue for understanding earthquake source physics and seismic activity in the Nankai subduction zone.

The effects of offshore heterogeneities on seismic wave propagation were investigated by

using both simulated seismograms and three-component broadband velocity seismograms of DONET stations. Simulated seismograms were evaluated at the same locations as the observational stations and virtual seafloor seismic stations, which were uniformly distributed at a horizontal interval of 0.05° in the model region. We used a parallel staggered-grid FDM code of OpenSWPC software (Maeda et al., 2017) to simulate seismic wave propagation of a shallow LFT and small regular earthquakes in the 3D viscoelastic medium. We employed the Cartesian coordinate system of Aki & Richards (2002), where x, y, and z are taken as north, east, and down, respectively. To avoid artificial reflections from model boundaries, perfectly matched layer boundary conditions (e.g., Zhang & Shen, 2010) were assumed at each model boundary.

The 3D velocity structure model developed by Koketsu *et al.* (2012) was used as the model beneath the bedrock. This model has been widely used for various applications across Japan (e.g., Furumura & Kennett 2018; Iwaki et al. 2018; Petukhin et al. 2016; Takemura et al. 2017, 2020). The ETOPO1 model (Amante & Eakins, 2009) was used as the topographic model in simulations. The 1D *S*-wave velocity structures beneath the DONET stations (Tonegawa et al., 2017) were used to model a 3D velocity structure within the accretionary prism. We converted the depth-varying velocity structure model of Tonegawa *et al.* (2017) to a 5-layer model beneath each DONET station. Extrapolation and interoperation of depths of the bottom of each layer via the '*Surface*' gridding algorithm of Generic Mapping Tools (Wessel et al., 2013) were applied to construct the 3D layered accretionary prism model (Figure S1). Details of the model construction are described in the Supporting Material (Text S1, Figures S1-S4). The *P*- and *S*-wave velocities, density (V_P, V_S, and ρ), and attenuations (Q_P and Q_S) for each layer are listed in Table 1. The minimum V_S of 0.5 km/s was assumed in the solid column. The 3D simulation model for shallow LFT and small earthquakes covered an area of 120 × 82.5 × 45 km^3 (delineated by the dashed-blue rectangle in Figure 2a), which was discretised by a grid interval of 0.015 km. Cross-sections of the constructed layered structure model are illustrated in Figures 2b and 2c. This model is the reference model. Simulations of high-frequency seismic wave propagation were conducted using calculation resources of the Earth Simulator at JAMSTEC. Each simulation required 24 TB of computer memory and a wall-clock time of 6.3 h by parallel computing using 1,280 nodes (5,120 cores) of the Earth Simulator to evaluate a seismic wave propagation of 60 s.

According to the observed seismic activity in this region, many intraslab earthquakes occurred at depths of 10–15 km and 20–30 km (e.g., Nakano et al., 2015; Sakai et al., 2005;

Takemura et al., 2020). Interplate earthquakes (~10 km), related with the 2016 southeast off Kii Peninsula earthquake, and shallow (< 7 km) slow earthquakes were also observed. Thus, we investigated the effects of 3D heterogeneities on seismic wave propagations from those three different hypocentres in our simulations (Table 2). Simulation results for earthquakes at different depths allowed us to investigate depth-dependent structural responses. Events A, B, and C occurred on 16 April 2016, 19 April 2016, and 4 December 2014, respectively. Because source parameters for events A–C were not precisely estimated, we assumed double-couple point sources of CMT solutions for the nearest shallow VLFE or moderate size earthquakes (Takemura et al. 2019, 2020). Although source durations of LFTs estimated in previous studies ranged from 10 to 30 s (e.g., Gomberg et al., 2016; Nakano et al., 2019; Yabe et al., 2019), the present source models all employed a simple triangle function duration of 0.2 s, which roughly corresponds to a duration of earthquakes with magnitudes of 3.

Before the analysis of simulated envelopes, we calculated the Fourier amplitude spectrums for both observed and simulated DONET (M.KMB07) seismograms for the 50 s time window that began at the origin time (Figure 3). The multi-radix fast Fourier transformation algorithm (Takahashi, 2013) was employed. Amplification due to the accretionary prism commonly appeared in low-frequency (0.1–0.2 Hz) components for a shallow LFT. Noise levels of observed seismograms around frequencies of 0.1–0.5 Hz were high due to secondary microseism (e.g., Nishida, 2017). The spectrum of a shallow LFT (red line) showed a weaker high frequency (> 2 Hz) component compared with regular earthquakes. However, spectrums of simulated seismograms showed similar levels for the high frequency (> 2 Hz) range. According to the comparison of Fourier spectrums, we note that a 0.1 s triangle function is unrealistic, especially for a shallow LFT case. However, simulation results of such an unrealistic and short duration STF provide opportunities for investigating the effects of structural heterogeneities on high-frequency seismic wave propagation in offshore regions. In other words, the effects of structural heterogeneities are important for source parameter estimation.

3. Simulation results

Figure 4 shows snapshots of the simulated *P*- and *S*-wave propagations of a shallow LFT. The *P*- and *S*-wavefields were evaluated by calculating the divergence and rotation, respectively, of the simulated velocity wavefield of a shallow LFT source. The *P* and *S* waves, which radiated from a shallow LFT on the plate boundary, showed complex

propagation through heterogeneous structures and repeating scattering and reflection from each layer boundary. The intensities of *P* and *S* waves at depths below the bedrock were very weak, but large seismic energies were trapped within the low-velocity accretionary prism. The *P* waves were also trapped within the seawater layer as ocean acoustic waves. According to these simulated *P* and *S* wavefields, long-duration complicated simulated seismograms can be expected.

The root-mean-square (RMS) envelopes for the shallow LFT simulation are shown in Figure 5a. After synthesizing three-component MS envelopes for the frequencies of 1–5 Hz, the RMS envelopes were evaluated by taking the mean square for the sum of the three-component MS envelopes. The RMS envelope was smoothed by taking the 1 s moving average. Because the FDM can evaluate the seismic wave propagation for frequencies less than 5 Hz due to our simulation settings, we investigated simulated seismograms for the 1–5 Hz frequency band, which is lower than the typical dominant frequencies of LFTs (2–8 Hz). After calculating the vector sum of three-component envelopes, a moving average with a time window of 1 s was applied. Each trace was normalized by each maximum amplitude. The envelopes at stations around the epicentre (< 10 km) clearly showed a short-duration *S*-wave pulse and weak later phases. However, as distance increased, RMS envelopes broadened rapidly. At distances greater than 30 km, the onsets of *S* waves were not clear and RMS envelopes were characterized by spindle shapes with durations of 20–30 s. These *S*-wave durations were significantly longer than the assumed source pulse (0.2 s). This broadening and delayed peak of simulated seismogram envelopes was much larger than for seismic waves propagating through the typical lithosphere (e.g., Saito et al., 2005; Takahashi et al., 2007; Tripathi et al., 2010).

On the other hand, the simulated RMS envelopes for regular earthquakes were composed of pulse-like *S* waves and multiple distinct later packets (Figures 5b and 5c). Multiple later packets may be developed by the seawater layer, accretionary prism, or subducting oceanic plate. The simulation of the deepest source (event C; Figure 5c) showed simpler RMS envelopes. Simulations of all events were conducted by using the same source time function (0.2 s triangle function), but the simulated envelopes for event A were very different from those for events B and C. Significant differences were found in simulated RMS envelopes between events A and B, despite similar source mechanisms, both of which were low-angle thrust faulting on the plate boundary. Thus, we considered that differences in simulated RMS envelopes between a shallow LFT and regular earthquakes could be caused by shallower

heterogeneous structures.

Figure 6 shows observed RMS envelopes of a shallow LFT on 16 April 2016, an interplate earthquake on 19 April 2016, and an intraplate earthquake on 4 December 2014. Because we did not know the precise source parameters of these small events and incorporated the effects of site amplification at each station, we compared the shapes of seismogram envelopes between simulations (Figure 5) and observations (Figure 6). Similar characteristics of simulated RMS envelopes were found in observations. Although the durations of observed RMS envelopes for a shallow LFT were longer than the simulation with a 0.2 s triangle function (Figure 5 a), the observed RMS envelopes also broadened with increasing distance (Figure 6a). Pulse-like wave packets of *S* waves and later phases appeared in observed RMS envelopes for regular earthquakes (Figures 6b and 6c). To quantify the similarity between observed and simulated envelopes, we calculated cross-correlation coefficients (CCs) between both envelopes. In calculations of CCs, we allowed time shifts within ±3 s because we did not know the precise source parameters for observed seismograms. Figure 7 shows spatial variations of cross-correlation coefficients for Events A–C. Due to sensor conditions, we discarded DONET E-node (northwest four stations) in the comparison for Event C. We confirmed high (> 0.7) correlation coefficients except for Event A. The cause of CCs for Event A can be explained by an assumed STF. The comparison of simulation with a complex STF is discussed in the later section. The CCs of RMS envelopes between simulations and observations suggest that our local 3D model reliably characterizes seismic wave propagation southeast off the Kii Peninsula, Japan.

Figure 8 shows the spatial variations of maximum RMS amplitudes and envelope half-value widths derived from ground motion simulation for a shallow LFT. The envelope half-value width is the period for which the amplitude is greater than half of the maximum amplitude (Figure 8a) and has been used to represent the event duration of LFTs (e.g., Ide, 2010; Yabe et al., 2019). We used simulated RMS envelopes at both DONET and virtual seismic stations for detailed evaluations of spatial variations in amplitude and duration. The simulated amplitude distribution did not show a simple two-lobe pattern, which was expected from the assumed source mechanism. Generally, the high-frequency maximum amplitude distribution is distorted from the expected source radiation pattern by seismic wave scattering and diffraction due to small-scale subsurface heterogeneities (e.g., Imperatori & Mai 2013; Morioka et al. 2017; Takemura et al. 2009, 2016). Because we did not introduce a small-scale velocity heterogeneity into the reference model in this simulation, we confirmed that the

shallower heterogeneities, such as seawater and the thick low-velocity accretionary prism, also distorted the maximum amplitude distribution. Thus, the assumption of isotropic radiation for energy estimations of small offshore seismic events in many studies could be suitable (e.g., Tamaribuchi et al., 2019; Yabe et al., 2019). Because our simulations did not include site amplifications caused by structures with $V_S < 0.5$ km/s, the observed maximum amplitude distribution could be more complicated because of site amplification factors at DONET stations for high-frequency seismic waves (e.g., Kubo et al., 2018; Yabe et al., 2019).

Figures 8c and 8d show spatial variations and distance-change properties of half-duration widths from the simulation results for a shallow LFT source. We also plotted the theoretical values of t_q via the method of Sato & Emoto (2018) as a typical envelope broadening for onshore earthquakes. Parameter t_q is defined as the time between *S*-wave onset and the time when the RMS envelope decays to half the maximum amplitude. This t_q value only reflect the effect of envelope broadening due to small-scale velocity heterogeneity. Typical t_q values in onshore regions gradually increase from 2 to 10 s at distances of 20–200 km (e.g., Tripathi et al., 2010). Although the half-value widths exhibited heterogeneous distribution and were widely scattered, these values increased with increasing distance and were of much longer duration than values of t_q (red lines). These longer and distance-dependent *S*-wave durations could be caused by shallower heterogeneous structures, such as seawater and the accretionary prism. Thus, to reliably estimate source duration, the effects of elongation due to shallower structures should be incorporated.

On the other hand, the half-value widths for a simulated interplate earthquake did not show clear distance-dependent properties (Figure 9). Some stations showed distinct reflection phases from the sea surface or bedrock (Figures 5b, 6b, and 9b). Similar features appeared in cases of an intraslab earthquake (Figure S5). Weak distance-dependent features were confirmed in half-value widths for later portions. Step-like elongation of half-value widths could be explained by multiple reflections from sea surface and bedrock boundary. Source durations of interplate earthquakes could be overestimated if such multiple reflections are counted as the durations of *S* waves. Conversely, by excluding such reflection phases and site amplifications from the analysis, the source parameters of offshore regular earthquakes, which occurred at sufficient depths below the accretionary prism, could be robustly estimated.

4. Effects of heterogeneous structures on source parameter estimation for small seismic events

4.1. Effects of heterogeneous structures on offshore seismograms

We demonstrated that high-frequency seismic waves show complicated propagation in offshore regions due to the influence of 3D heterogeneous structures. Our model in previous 3D simulations contains seawater, low-velocity accretionary prism, crust, and the subducting Philippine Sea plate. According to the snapshots of the simulated wavefield and differences in simulated envelopes due to source locations, shallower heterogeneities could strongly affect high-frequency seismic wave propagation. Shallower heterogeneities affect the maximum amplitude distribution and envelope broadening of high-frequency seismic waves. At frequencies greater than 1 Hz, characteristics of seismic wave propagation were usually affected not only by deterministic layered structures but also small-scale velocity heterogeneities along the propagation path (summarized in Ch. 2 of Sato et al., 2012). In this sub-section, we discuss the effects of a small-scale velocity heterogeneity, seawater, and low-velocity accretionary prism on high-frequency seismic wave propagation through offshore regions.

Small-scale velocity heterogeneities were modelled by using stochastic random velocity fluctuations characterized by an exponential autocorrelation function (ACF). The parameters of small-scale velocity heterogeneity (correlation length and RMS value) within the slab mantle and others were derived from Furumura & Kennett (2005) and Takemura et al. (2017), respectively (see Table 3). We assumed the small-scale velocity heterogeneity within the accretionary prism as the same as that within the crust. Similar small-scale heterogeneity models were previously used for waveform modelling in the Kanto sedimentary basin (Takemura & Yoshimoto 2014).

We employed the following four heterogeneous models to evaluate the effects of each heterogeneity on offshore seismograms: model with a small-scale velocity heterogeneity; model without a seawater layer; model without an accretionary prism; and model without a seawater layer and accretionary prism. The model with a small-scale velocity heterogeneity was constructed by superposing small-scale velocity heterogeneities (in Table 3) on the reference model. In the model without the seawater layer, the physical parameters within the seawater layer were replaced with those within the air column, and the seafloor was treated as the free surface. In the model without the low-velocity accretionary prism, physical parameters were replaced with those of the upper crust (Table 1). All models included

bathymetry, but we do not discuss its effects because previous studies have reported limited effects of topographic scattering on body wave propagation (e.g., Imperatori & Mai, 2015; Takemura et al., 2015).

Figure 8 shows the simulated RMS envelopes at DONET stations using the four different heterogeneous models. To visualize the effects of heterogeneities, RMS envelopes of the reference model were also plotted by grey lines. Although maximum amplitudes and later phases were slightly changed by introducing small-scale velocity heterogeneities, these effects were not significant (Figure 10a). This tendency remained unchanged when using stronger models or those with different random seeds (Figure S6). The durations of RMS envelopes also showed slight differences between models with/without small-scale velocity heterogeneities (Figure S7). In typical crustal earthquakes, the effects of small-scale velocity heterogeneity appear as amplitude fluctuations of high-frequency seismic waves even for stations at shorter distances (e.g., Yoshimoto et al., 2015). Numerical simulations by Iwaki et al. (2018) showed that crustal small-scale heterogeneity has limited effects on ground motions for frequencies lower than 1 Hz in the Kanto sedimentary basin. Our large-scale simulations demonstrate that the effects of the sedimentary layers (accretionary prism) on high-frequency seismic waves are stronger than those of small-scale velocity heterogeneities.

In the model without seawater, the seafloor was treated as the free surface, and consequently, RMS amplitudes were amplified (Figure 10b). The low-velocity accretionary prism has dominant effects on high-frequency seismic waves in this region. The model without the accretionary prism exhibited simple pulse-like RMS envelopes, which were very similar to the typical envelopes of onshore small earthquakes (Figure 10c). Pulse-like *S* waves and multiple small pulses after *S* waves were found in simulated RMS envelopes. The differences between the RMS envelopes of the reference model and the model without the accretionary prism indicate that elongations of *S* waves at offshore stations were mostly caused by the low-velocity accretionary prism.

Multiple later packets after *S* waves were weak but also present in the RMS envelopes of the model without both seawater and an accretionary prism (Figure 10d). These phases could be interpreted as reflections from the subducting Philippine Sea slab. It was difficult to find the phases reflected from the subducting Philippine Sea slab in the RMS envelopes of the model that included the accretionary prism, as the elongation and amplification effects of the accretionary prism masked reflections from the Philippine Sea plate. Tonegawa et al. (2015) also reported that reflections from the bedrock (bottom of oceanic sediments) are also

dominant in ambient noise wavefields, and it can be difficult to identify reflections from the boundaries at depths below the bedrock.

According to the above results, we conclude that the low-velocity accretionary prism is the dominant influence on high-frequency seismic wave propagation through the offshore region, whereas other heterogeneities, such as seawater and small-scale velocity heterogeneities, have minor effects. Similar tendencies were also found in simulations of interplate and intraslab earthquakes (Figures S8 and S9). The low-velocity accretionary prism is also important for low-frequency surface wave propagation (e.g., Takemura, Kubo, et al. 2019; Volk et al. 2017). Strong amplification or waveguide effects for both low- and high-frequency seismic waves due to the accretionary prism were also reported in the Cascadia, Mexico, and Hikurangi subduction zones (e.g., Gomberg, 2018; Kaneko et al., 2019; Shapiro et al., 2000). To achieve reliable modelling of broadband seismic wave propagation through offshore regions, and precise source-parameter estimations for offshore seismic events, a detailed model of the low-velocity accretionary prism should be considered.

4.2. Source parameter estimation for a shallow LFT via the conventional method

For small events, especially LFTs, the durations, source energies, or band-limited moments have been estimated by using stacked coherent RMS envelopes or average values for the used stations after correction of site amplification and attenuations (e.g., Annoura et al., 2016; Ghosh et al., 2009; Kao et al., 2010; Maeda & Obara, 2009; Yabe et al., 2019; Yabe & Ide, 2014). However, our simulations demonstrated that elongation of RMS envelopes for a shallow LFT, due to the low-velocity accretionary prism, occurs even for stations as close as 10 km from the epicentre (Figures 5a and 8). Thus, incorrect estimation of source parameters via the conventional method can be expected. In this sub-section, we conducted an FDM simulation of seismic wave propagation and compared it with observed RMS envelopes to investigate the validity and limitations of STFs estimation by the conventional method.

We used observed DONET seismograms for a shallow LFT that occurred at 11:18 on 24 October 2015 (JST), located at 136.91°E, 33.35°N. For deep slow earthquakes, the proportionality between seismic energy rate functions estimated from high-frequency seismograms and seismic moment rate functions estimated from low-frequency seismograms has been confirmed (Ide et al., 2008). Yabe et al. (2019) showed that the same proportionality holds true for shallow slow earthquakes. Therefore, seismic energy rate functions estimated

410 from high-frequency seismograms can be converted into STFs by dividing them by the value
411 of scaled energy. The seismic energy rate function of the event observed at each station is
412 conventionally calculated from squared seismograms at each station after correction of site
413 and attenuation effects within time windows of half-value width measured for the stacked
414 RMS envelope. Seismograms were excluded from the analysis if the cross-correlation
415 coefficient with the same event envelopes at any other stations did not exceed 0.6. This
416 procedure removed stations lacking tremor signals. Modelling for direct-*S* wave energies
417 using the uniform background velocity structure (V_S = 3.5 km/s and ρ = 2700 kg/m^3) and
418 distance-dependent attenuation model (Figure 3 of Yabe et al., 2019) was employed. The
419 seismic energy rate functions were converted into STFs by assuming a scaled energy value of
420 3.0×10^{-9} (Ide & Maury, 2018; Ide & Yabe, 2014; Yabe et al., 2019). The STF of the event
421 was calculated by stacking STFs at each station after applying a 10 s low-pass filter.
422 Figure 11 shows the STFs of a shallow LFT that occurred on 24 October 2015. The
423 conventional method typically provided STFs represented by blue dashed or red lines, which
424 were estimated by using stacking seismic energy rate functions of B-node stations and B- and
425 C-node stations, respectively. The moment releases of these STFs continued 50–60 s from the
426 origin and peaks of moment rate appeared at around 25 s. The STF described by the solid-
427 blue line was constructed by using the seismic energy rate function at M.KMB06 only, which
428 was located just above the shallow LFT hypocentre. This STF was completely different from
429 the others. The peak of this STF appeared within 3.2 s of the origin, and the moment release
430 continued 30–40 s from the origin. By using these STFs, we synthesized seismograms of the
431 shallow LFT. Hypocentre depth was fixed on the plate boundary, and the focal mechanism
432 was the same as in previous simulations of event A (Table 2). After FDM simulations, we
433 convolved the estimated STFs to simulated envelopes. To achieve suitable STF convolutions,
434 we assumed a simple 0.1 s triangle function, which was sufficiently shorter than the STFs in
435 Figure 11. After FDM simulations, we convolved the estimated STFs to simulated envelopes.
436 Figure 12 compares 1–5 Hz RMS envelopes between simulations and observations. In this
437 comparison, the amplitudes of each trace were normalized by each maximum amplitude
438 because the precise seismic moment and site amplification factors from the V_S = 0.5 km/s
439 layer were not well known. The analysis focused on differences in envelope shapes between
440 simulations and observations. To quantify fitness of envelope shapes, we also calculated CCs
441 between observed and simulate envelopes (blue numbers in each trace). The simulation
442 results with the STF from M.KMB06 reproduced the observed envelope shapes and durations

443 at all stations. Almost all of the simulated envelopes had CCs larger than 0.7. This STF also
444 reproduced the seismograms observed for a shallow VLFE (Yabe et al., 2019), which
445 occurred in the same time window as the target shallow LFT but appeared for frequencies of
446 0.03–0.05 Hz.
447 The simulations with the other STFs were much longer than the observations. Two of the
448 simulated STFs also showed delayed peak amplitudes compared to the observations. The
449 epicentral distances of B-node stations except for M.KMB06 ranged from 10 to 16 km. The
450 simulation with a simple STF (Figures 5a and 8) demonstrated that the durations of *S* waves
451 increased rapidly with increasing distance, and values reached to 5–15 s at stations located at
452 distances of 10–15 km. Thus, STFs from stacked seismic energy rate functions via the
453 conventional method were delayed and overestimated. The simulation with a simple STF of
454 duration 0.2 s (see Figure 5a) shows that the RMS envelopes at very close (< 10 km) stations
455 are characterized by a pulse-like *S* wave packet, and consequently, seismic energy rate
456 functions at close stations could preserve source information. Thus, the shapes and durations
457 of observed RMS envelopes were only well reproduced in the STF estimated from the nearest
458 station (~1.4 km, M.KMB06).
459 Our numerical tests in this sub-section revealed that STFs from stations very close to the
460 source reproduced the observed seismogram envelops of the target shallow LFT. In other
461 words, the effects of offshore heterogeneities were limited at stations with epicentral
462 distances less than 10 km, even for shallower (~5 km) seismic events (see Figure 5), and,
463 consequently, the source parameter information could be preserved. At stations with
464 epicentral distances greater than approximately 10 km, RMS envelopes were strongly
465 elongated due to the effects of the accretionary prism (Figure 5a). At stations with epicentral
466 distances greater than approximately 10 km, durations of the RMS envelope were controlled
467 by the heterogeneous structure of the accretionary prism along the propagation path. Thus,
468 STFs calculated by using such stations via the conventional method (e.g., Yabe et al., 2019)
469 were overestimated and could not reproduce the observed RMS envelopes. When the
470 conventional method is applied to OBS data, seismograms should be selected from stations
471 located closer than approximately 10 km. If stations further than 10 km from the source are
472 used, the effects of 3D offshore heterogeneities should be included in the method of source
473 parameter estimation.
474
475 **5. Conclusions**

476 We investigated the effects of offshore heterogeneities, such as a small-scale velocity
477 heterogeneity, seawater, and the accretionary prism, on high-frequency seismic propagation
478 southeast off the Kii Peninsula, southwest Japan. Our simulations demonstrated that the low-
479 velocity accretionary prism affects the shapes of seismogram envelopes. A thick low-velocity
480 accretionary prism is also developed in the Cascadia, Mexico, and Hikurangi subduction
481 zones, and this affects not only low-frequency surface waves, but also high-frequency seismic
482 waves. The effects of the accretionary prism are significant for shallow-depth events along
483 the plate boundary, which correspond to shallow LFTs along the Nankai Trough, as these
484 sources are typically located just beneath the accretionary prism toe at depths of 5–8 km near
485 the trench axis. On the other hand, seismogram envelopes for sufficiently deep-depth events,
486 which correspond to interplate and intraslab regular earthquakes along the Nankai Trough,
487 comprise multiple pulse-like wave packets that consist of direct-*S* waves and multiple
488 reflections from the bedrock.
489 The seismogram envelopes of a source at shallow LFT depths (5–7 km) were broadened
490 due to the low-velocity accretionary prism, even when assuming a simple STF. The durations
491 of RMS envelopes exceeded 10 s, even at stations located at distances greater than 10 km.
492 Multiple reflected phases found in seismograms of regular earthquakes also can affect half-
493 value widths. Such elongation of envelopes will cause incorrect estimations of event
494 durations. Event durations are important for discussing the scaling law of regular and slow
495 earthquakes. After removing such reflection phases and site amplification from the analysis,
496 the source parameters of offshore regular earthquakes, which occurred at sufficient depths
497 below the accretionary prism, could be reliably estimated.
498 At stations very close (< 10 km) to the source, pulse-like *S* wave envelopes, reflecting an
499 assumed STF, were preserved for shallow (5–30 km) small seismic events. If stations at
500 distances greater than 10 km are used, the STF could be overestimated in terms of the
501 duration and peak time of the moment rate. By estimating the STF by using only the nearest
502 stations, the FDM simulations reproduced the shapes and durations of observed RMS
503 envelopes. Thus, conventional approaches might work well by using stations at distances less
504 than 10 km.
505 High-frequency seismogram envelopes are useful for both studies of structural property
506 (e.g., Carcolé & Sato, 2010; Przybilla et al., 2009; Saito et al., 2005; Takemura et al., 2015)
507 and source parameter estimations (e.g., Battaglia & Aki, 2003; Gusev & Pavlov, 1991; Ide et
508 al., 2008; Yabe et al., 2019). Envelope based source inversions have been conducted by using

theoretical Green's function envelopes (e.g., Nakahara, 2013; Petukhin et al., 2004; Sawazaki & Enescu, 2014).Theoretical envelopes can be easily evaluated, but 3D heterogeneous structures cannot be incorporated. Combined use of the Green's functions of numerical simulations in a 3D local model and site amplifications due to lower (V_S < 0.5 km/s) velocity sediments at each station can potentially enable reliable source parameter estimations even for small offshore events. Green's functions within the local layered model are also useful for estimations of small-scale heterogeneities within oceanic sediments, which may reflect physical properties or clack distributions of the accretionary prism. Such challenging work remains for future studies.

Acknowledgements

F-net and DONET waveform data are available via the NIED website (https://doi.org/10.17598/NIED.0005, https://doi.org/10.17598/NIED.0008). Bathymetric depth data were obtained from ETOPO1 (Amante & Eakins, 2009). OpenSWPC software (Maeda et al., 2017) and the 3D model of Koketsu et al. (2012) were obtained from https://doi.org/10.5281/zenodo.3712650 and https://www.jishin.go.jp/evaluation/seismic_hazard_map/lpshm/12_choshuki_dat/, respectively. Generic Mapping Tools (GMT; Wessel et al., 2013) and Seismic Analysis Code (SAC; Helffrich *et al.* 2013) were used to produce the figures and in signal processing, respectively. The multi-radix FFT package (ffte; Takahashi, 2013) is available at http://www.ffte.jp/. The catalogues of slow earthquakes (Nakano, Hori, *et al.* 2018, Takemura *et al.* 2019) were downloaded from the Slow Earthquake Database website (Kano et al., 2018; http://www-solid.eps.s.u-tokyo.ac.jp/~sloweq/). The CMT results of the 2016 southeast off Kii Peninsula earthquake, Japan, and an intraslab earthquake used in regular earthquake simulations are available from https://doi.org/10.5281/zenodo.3523583. We also used the unified hypocentre catalogue of the Japan Meteorological Agency (https://www.data.jma.go.jp/svd/eqev/data/bulletin/index.html). The FDM simulations of seismic wave propagation were conducted by using the Earth Simulator of JAMSTEC. This study was supported by the Japan Society for the Promotion of Science (JSPS) KAKENHI Grant Numbers 17K14382, 18K13639 in the Grant-in-aid for Young Scientists and Grant Number 19H04626 in the Scientific Research under Innovative Areas 'Science of Slow Earthquakes'. We would like to thank Editage (www.editage.com) for English language editing. We also thank three anonymous reviewers and Editor Prof. J. Virieux for carefully reviewing the study and providing constructive comments, which have helped to improve the manuscript.

Tables

Table 1. Physical parameters of each layer in the 3D velocity structure model. The parameters were obtained from the Japan Integrated Velocity Structure Model (JIVSM) (Koketsu et al., 2012). The air and seawater layers were treated as being the same, following Maeda *et al.* (2017).

	V_P [km/s]	V_S [km/s]	ρ [kg/m^3]	Q_P	Q_S
Air	0.0	0.0	0.001	10^{10}	10^{10}
Seawater	1.5	0.0	1.04	10^6	10^6
Sedimentary layer 1	1.8	0.5	1.95	170	100
Sedimentary layer 2	2.2	0.8	2.07	272	160
Sedimentary layer 3	2.4	1.0	2.15	340	200
Sedimentary layer 4	3.0	1.5	2.25	510	300
Sedimentary layer 5	3.5	2.0	2.35	680	400
Basement	5.5	3.2	2.65	680	400
Upper crust	5.8	3.4	2.70	680	400
Lower crust	6.4	3.8	2.80	680	400
Upper mantle	7.5	4.5	3.20	850	500
Philippine Sea plate					
Oceanic crust layer 2	5.0	2.9	2.40	340	200
Oceanic crust layer 3	6.8	4.0	2.90	510	300
Oceanic mantle	8.0	4.7	3.20	850	500

552 **Table 2**. Source parameters used in FDM simulations. A shallow LFT and intraslab
553 earthquakes were referred from the nearest shallow VLFE and intraslab earthquakes of
554 CMT solutions in our previous studies (Takemura, Okuwaki, *et al.* 2019, Takemura *et al.*
555 2019). Double-couple point sources were assumed. The value of T_0 represents the STF
556 duration.

	Type	Lon. [E°]	Lat. [°N]	Depth [km]	Strike [°]	Dip [°]	Rake [°]	*Mw*	T_0 [s]
A	LFT	136.90	33.20	6.20	255.0	7.0	116.0	3	0.2
B	Interplate earthquake	136.34	33.40	11.15	243.3	10.1	114.4	3	0.2
C	Intraslab earthquake	137.11	33.28	28.7	264.3	37.9	37.9	3	0.2

557

558 **Table 3**. Parameters of small-scale velocity heterogeneities in each layer. The models of the
559 crust and oceanic crust were assumed to be the same as the model of crustal
560 heterogeneity (Takemura *et al.* 2017). The model of the oceanic mantle was derived from
561 Furumura & Kennett (2005).

Layer	ACF-type	Correlation length *a*	RMS value ε
Air and seawater	-	-	-
Accretionary prism	Exponential	Isotropic: 1 km	0.03
Crust	Exponential	Isotropic: 1 km	0.03
Mantle	-	-	-
Oceanic crust	Exponential	Isotropic: 1 km	0.03
Oceanic mantle	Exponential	Horizontal: 10 km Vertical: 0.5 km	0.03

562

563

Figures

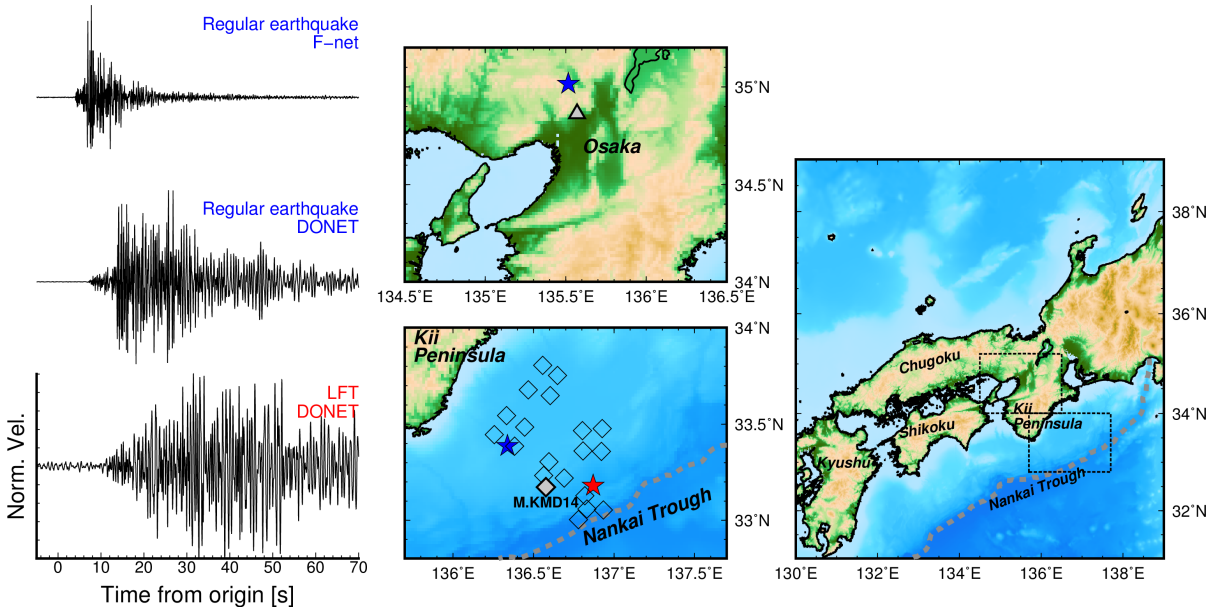

Figure 1. Examples of observed NS-component seismograms for a crustal earthquake, an offshore interplate earthquake, and a shallow LFT. Crustal and offshore interplate earthquakes occurred on 24 January 2015 and 1 April 2016, respectively. A shallow LFT occurred on 3 April 2016. The magnitudes of these events were approximately 3, and epicentral distances were also similar. The blue stars and red star in enlarged maps are the epicentres of regular earthquakes and the shallow LFT, respectively. The triangle and diamond symbols show the locations of the F-net and DONET stations, respectively.

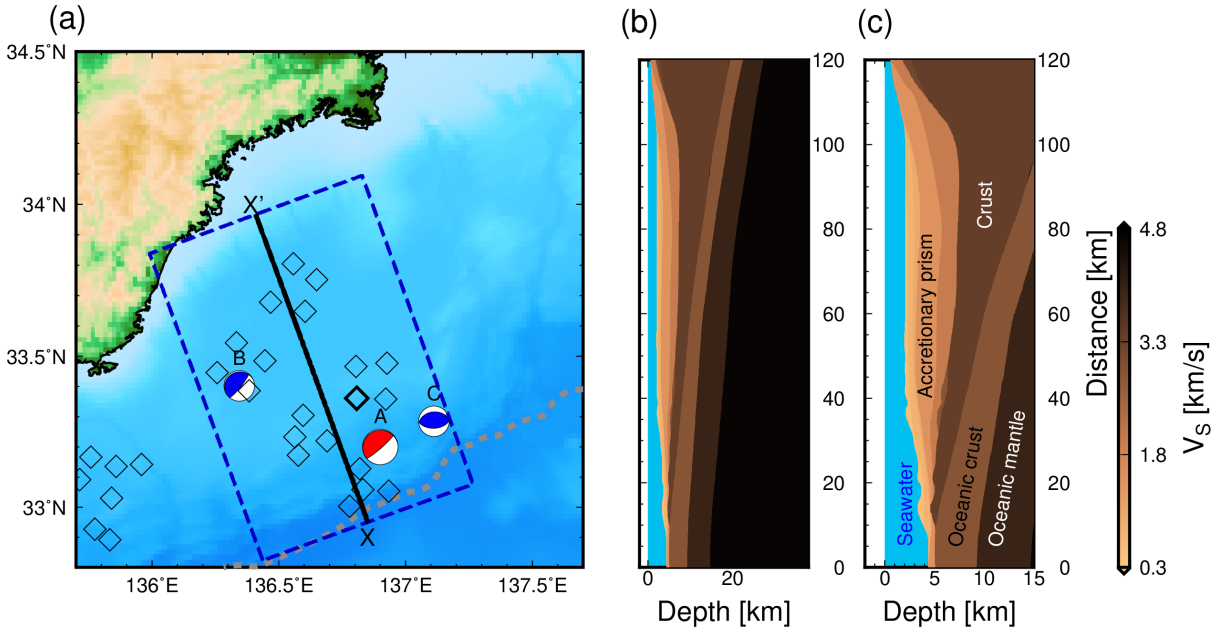

Figure 2. (a) Map of the simulation region, and cross-sections of the (b) *S*-wave velocity model along the X—X′ profile and (c) *S*-wave velocity model at shallower (< 15 km) depths. The red and blue focal mechanisms are source models of a shallow LFT and regular earthquakes, respectively. Details of physical parameters in each layer are listed in Table 1.

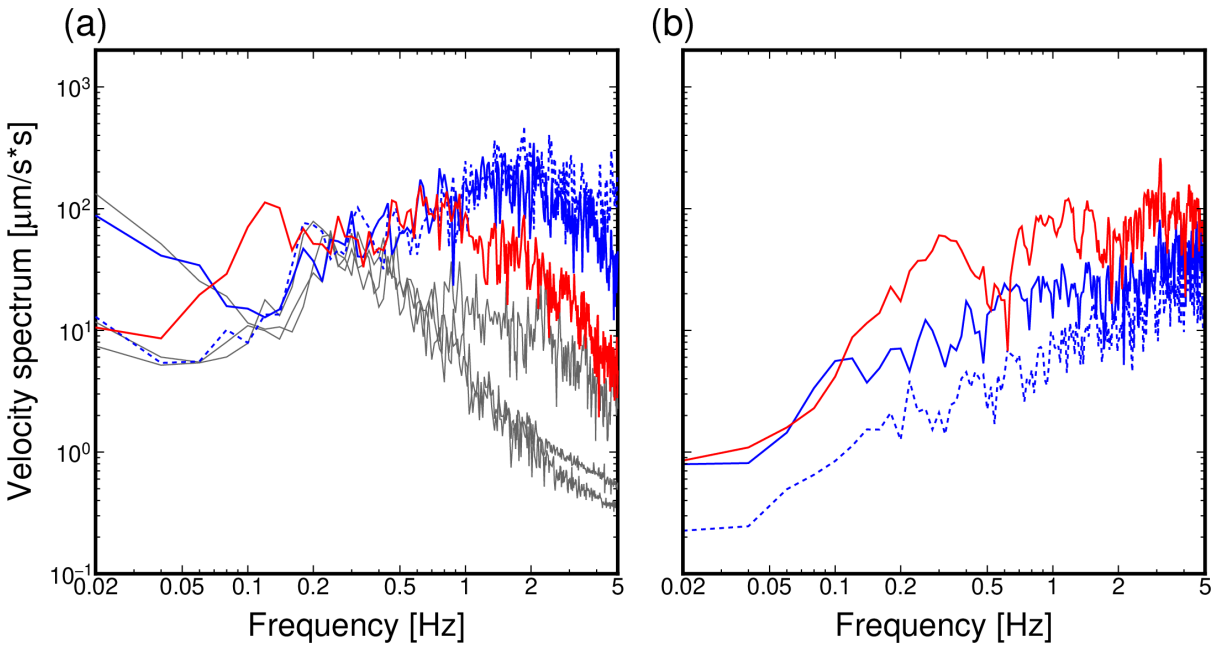

583

584 **Figure 3**. Fourier spectrums of (a) observed and (b) simulated seismograms at M.KMB07.
585 The location of M.KMB07 is shown in Figure 2 (bold diamond). The red, blue solid,
586 blue dashed, and grey lines in (a) are spectrums of a shallow LFT on 16 April 2016, an
587 interplate earthquake on 19 April 2016, an intraplate earthquake on 4 December 2014,
588 and noise parts, respectively. The red, blue, and blue dashed lines in (b) are spectrums of
589 simulated seismograms for Events A–C. The time window for the event signal is from
590 the origin time to the lapse time of 50 s.

591

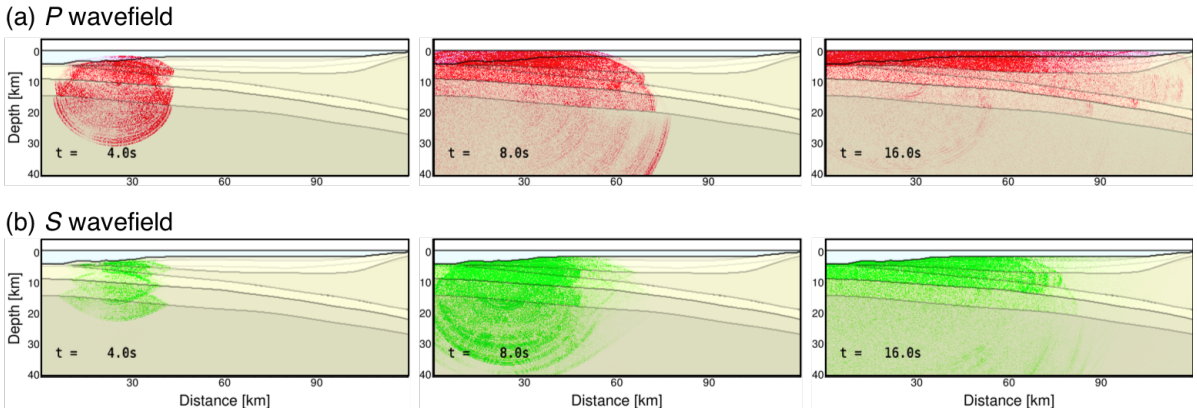

592

593 **Figure 4**. Simulated snapshots of (a) *P* and (b) *S* wavefields along profile X—X′ for the
594 shallow LFT simulation (red focal sphere in Figure 2).

595

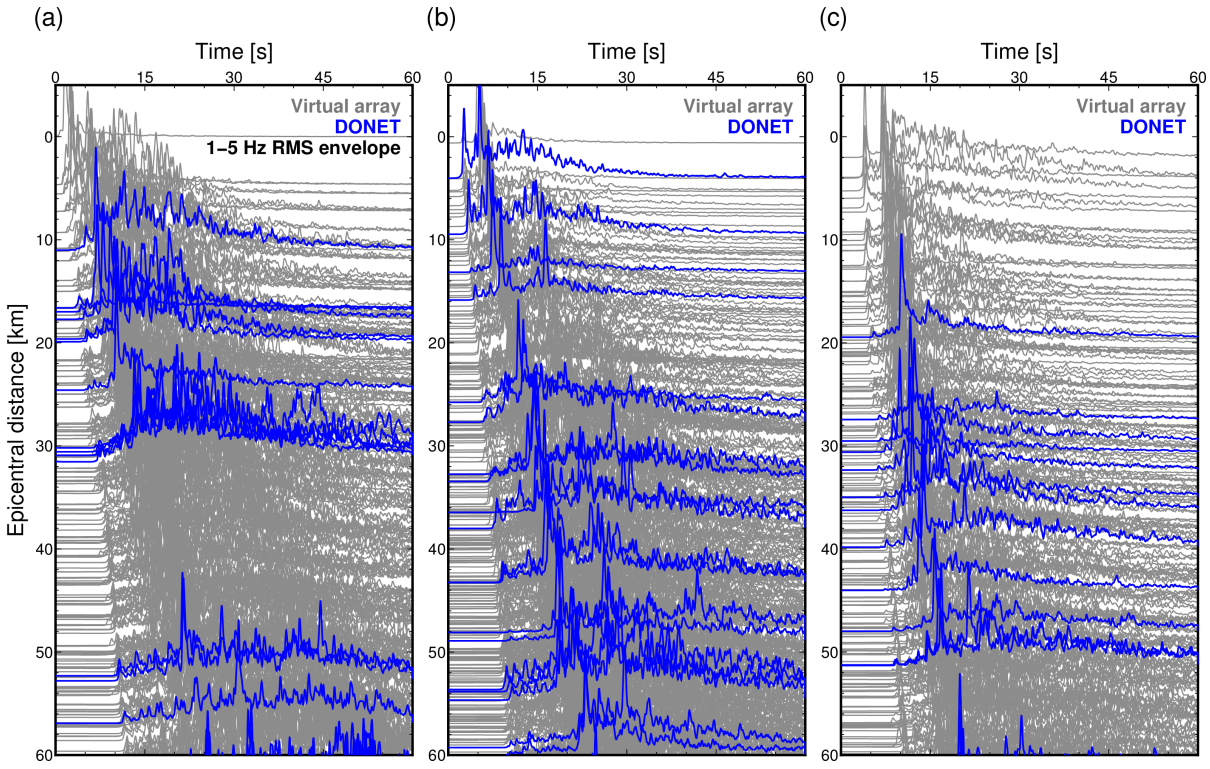

596

597 **Figure 5.** Simulated RMS envelopes for frequencies of 1–5 Hz from simulations of the (a)
598 shallow LFT, (b) interplate earthquake, and (c) intraslab earthquake. Source parameters
599 and locations are shown in Table 2 and Figure 2a. The RMS envelopes at DONET and
600 virtual stations are represented by blue and grey lines, respectively.

601

602

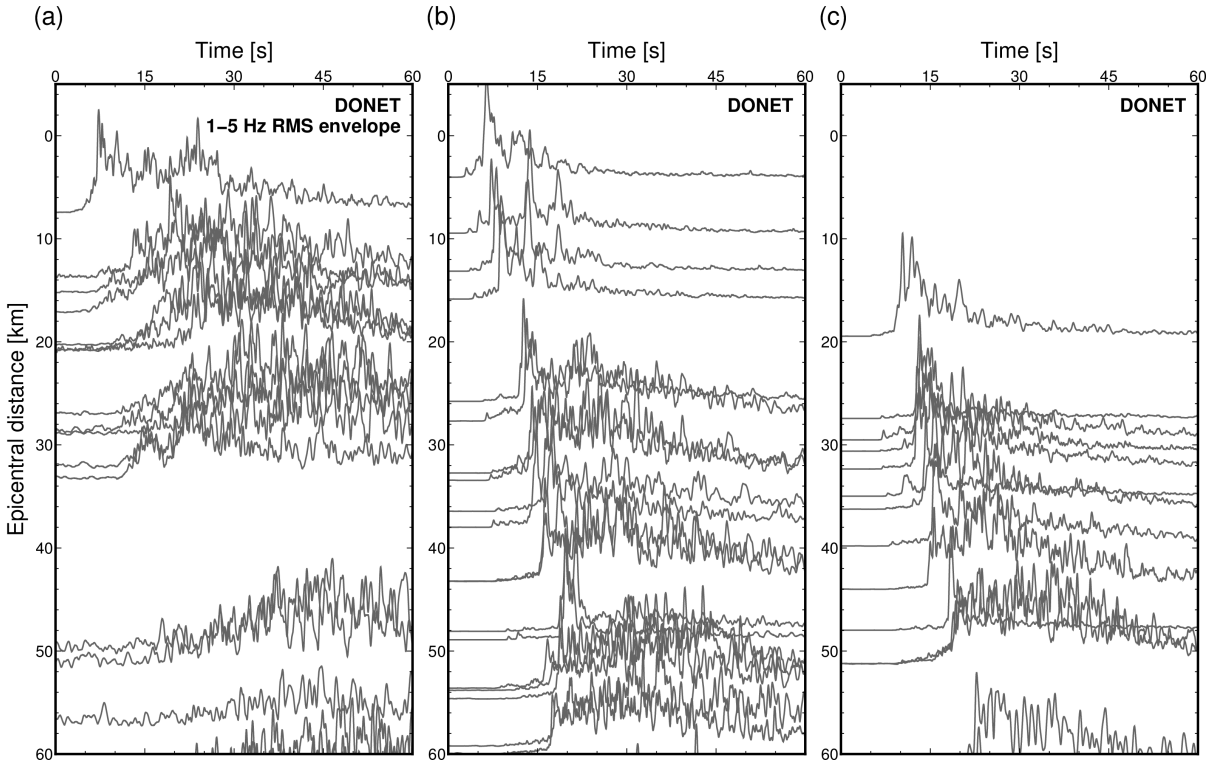

Figure 6. Observed RMS envelopes for frequencies of 1–5 Hz at DONET stations. The RMS envelopes for (a) a shallow LFT on 16 April 2016, (b) an interplate earthquake on 19 April 2016, and (c) an intraplate earthquake on 4 December 2014.

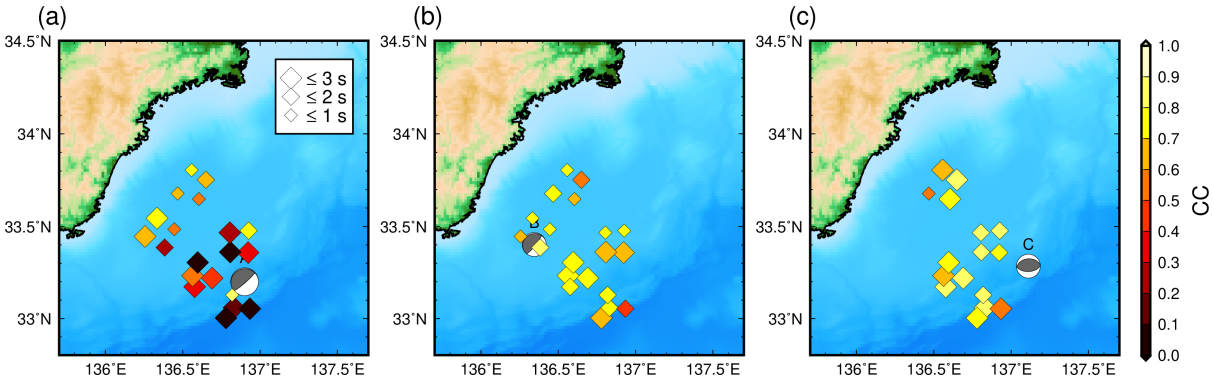

Figure 7. Spatial variations of cross-correlation coefficients between observed and synthesized envelopes for (a) Event A, (b) Event B, and (c) Event C. The sizes of symbols represent the absolute values of time shifts, which provide maximum correlation coefficients at each station.

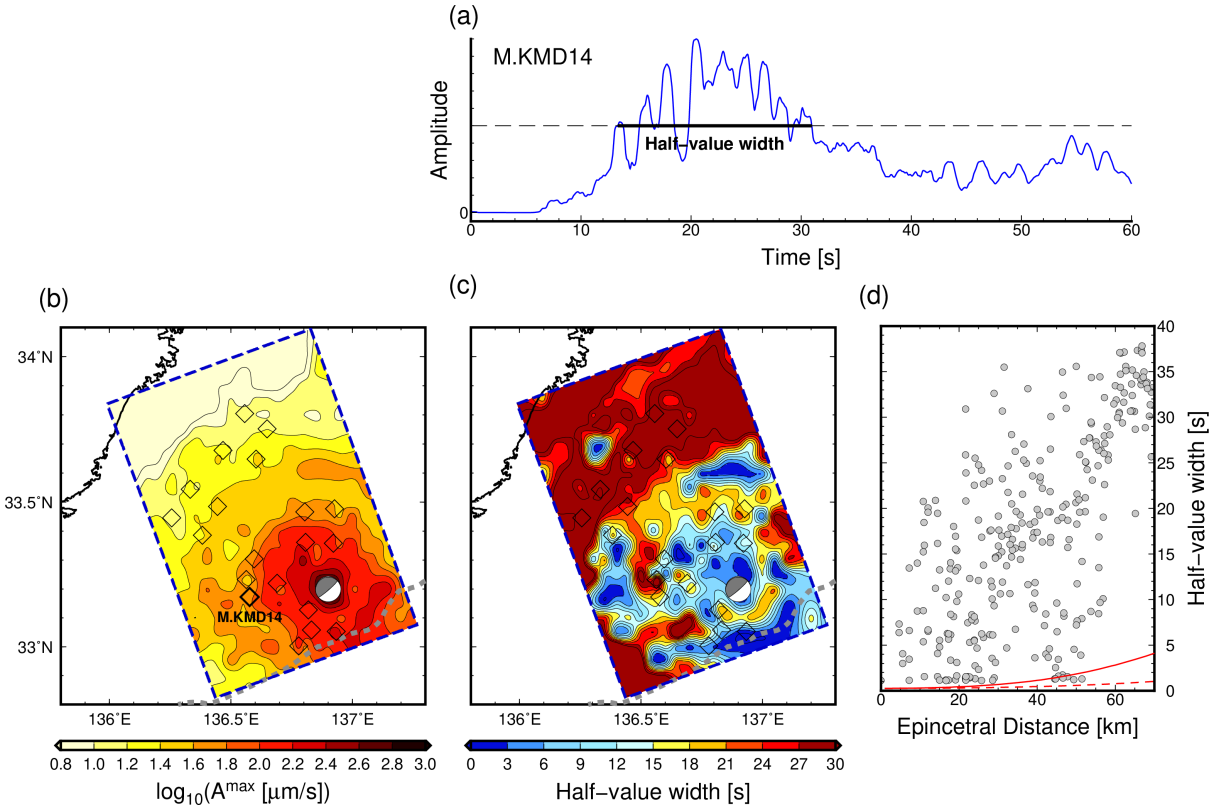

Figure 8. Spatial variations of maximum RMS amplitudes and half-value widths of simulated RMS envelopes for a shallow LFT: (a) an example of half-value width estimations, (b) maximum RMS amplitude distribution, (c) half-value width distribution, and (d) half-value widths as a function of the epicentral distance. The example in (b) is an RMS envelope at M.MRD14 (location shown in (a)). The red dashed and solid lines in (d) are values of t_q via the method of Sato & Emoto (2018). Here, t_q is defined as the time between *S*-wave onset and the time when the RMS envelope decays to half the maximum amplitude. The assumed small-scale random velocity heterogeneity models for dashed and solid lines are characterized by an exponential-type autocorrelation function with correlation length of 1 km and RMS values of 0.03 and 0.05, respectively. The central frequency in theoretical synthetics is 4 Hz.

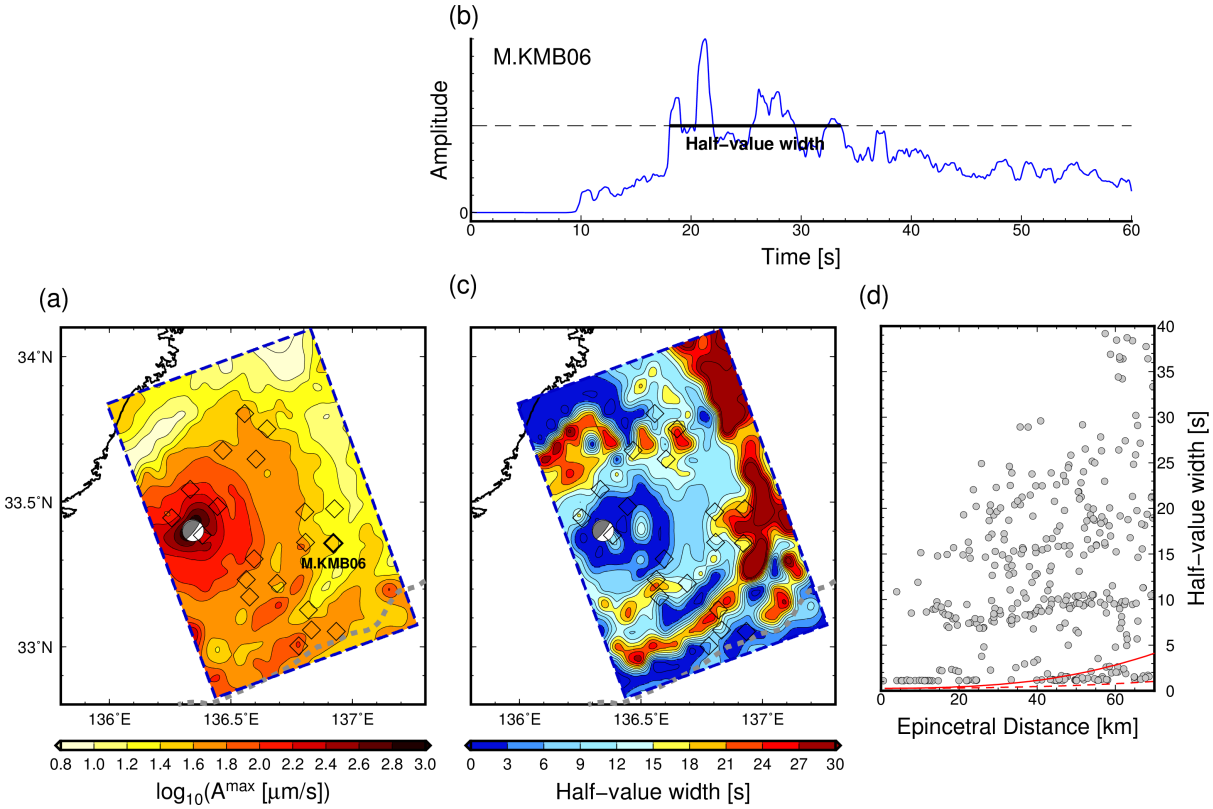

Figure 9. Spatial variations of maximum RMS amplitudes and half-value widths of simulated RMS envelopes for an interplate earthquake: (a) an example of half-value width estimations, (b) maximum RMS amplitude distribution, (c) half-value width distribution, and (d) half-value widths as a function of epicentral distance. The example in (b) is an RMS envelope at M.MRB06 (location shown in (a)). The red dashed and solid lines in (d) are values of t_q via the method of Sato & Emoto (2018). Here, t_q is defined as the time between *S*-wave onset and the time when the RMS envelope decays to half the maximum amplitude. The assumed small-scale random velocity heterogeneity models for dashed and solid lines are characterized by an exponential-type autocorrelation function with correlation length of 1 km and RMS values of 0.03 and 0.05, respectively. The central frequency in theoretical synthetics is 4 Hz.

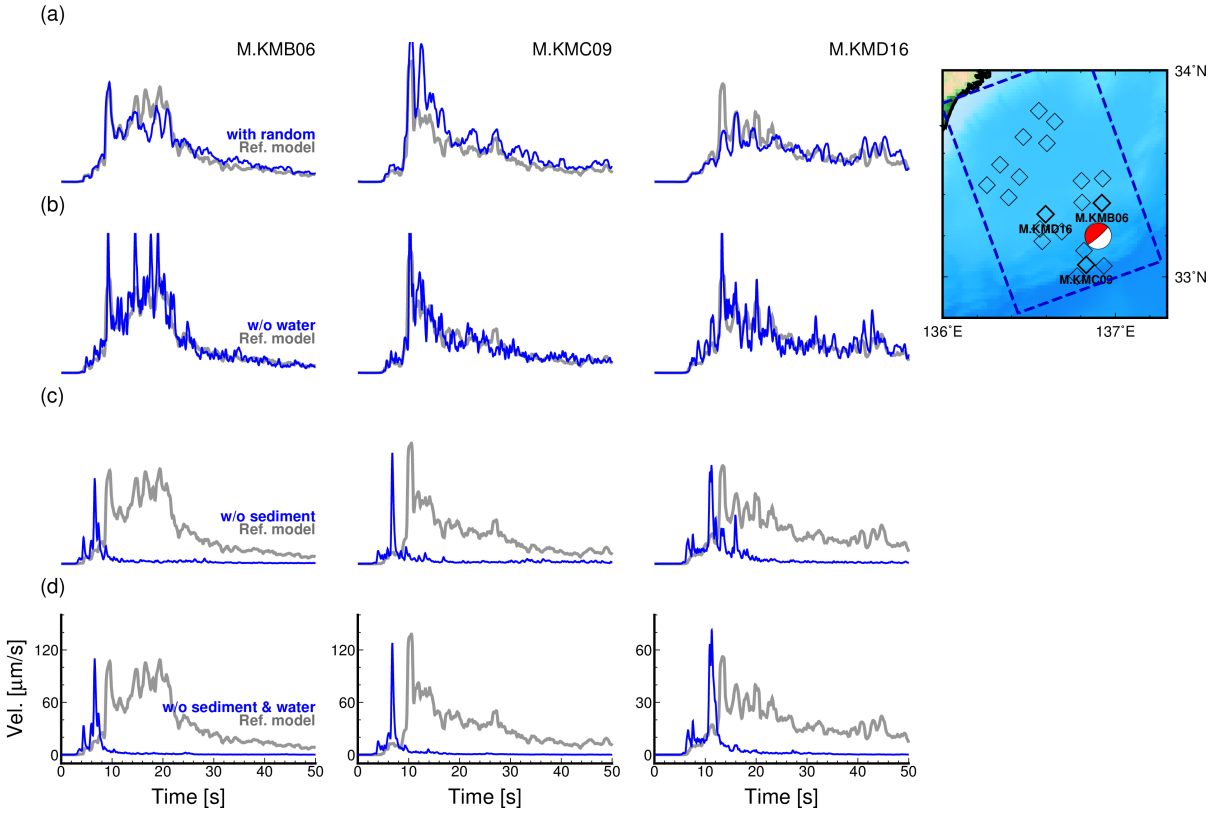

Figure 10. Simulation results for various heterogeneous models of a shallow LFT. The blue lines are RMS envelopes derived from models (a) with small-scale random velocity heterogeneities, (b) without seawater, (c) without oceanic sediments (accretionary prism), and (d) without oceanic sediments and seawater. Grey lines are the simulation results with the reference model.

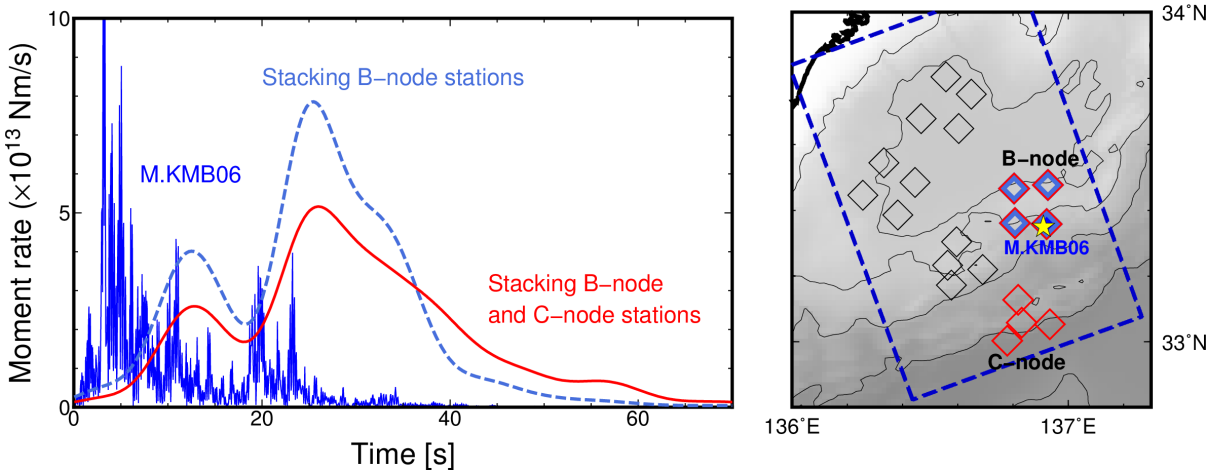

Figure 11. Source time functions (STFs) estimated from observed RMS envelopes of a shallow LFT at 11:18 on 24 October 2015 (JST). The blue dashed, blue, and red lines are source time functions estimated from the RMS envelope of M.KMB06, envelopes of B-node stations, and envelopes of B- and C-node stations, respectively. The yellow star on the map is the epicentre. The epicentral distance of M.KMB06 was 1.4 km. The stations represented by coloured symbols were used in the STF estimation for corresponding coloured lines.

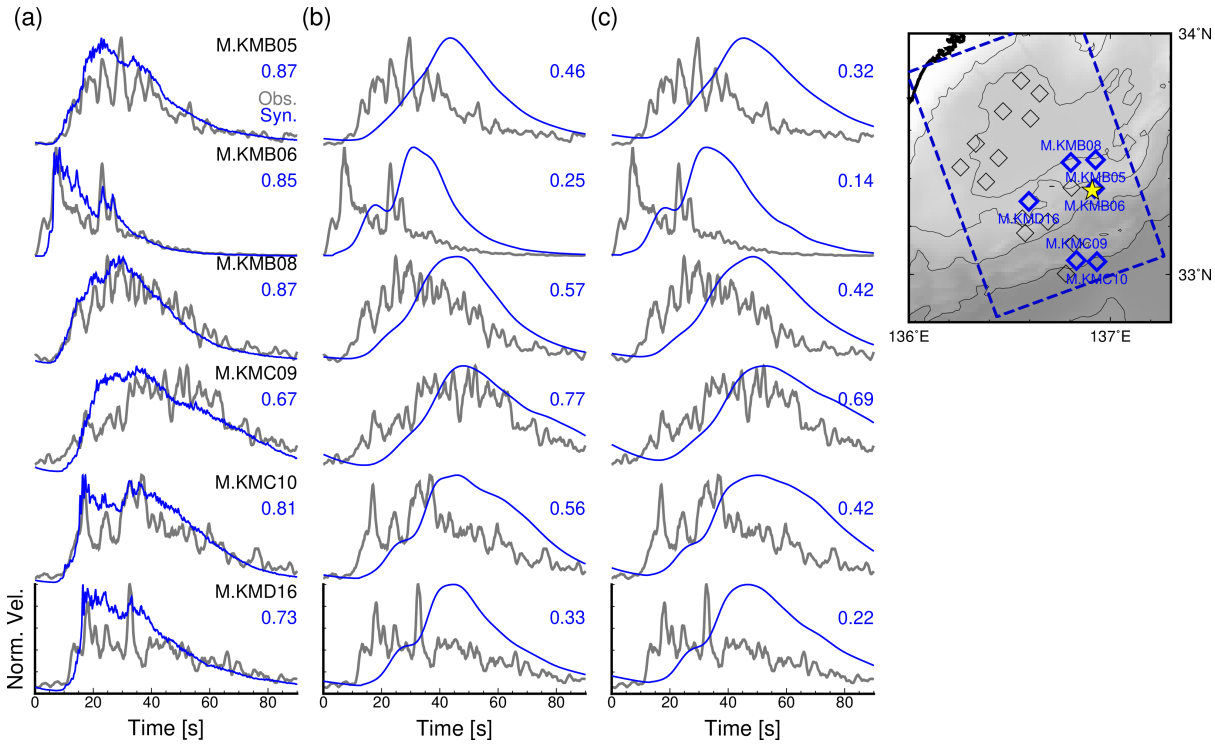

Figure 12. Comparison between simulated RMS envelopes with observations. The RMS envelopes were synthesized from simulation results of source time functions estimated by using (a) M.KMB06, (b) B-node stations, and (c) B- and C-node stations. Because the precise seismic moment for the target shallow LFT and site amplification factors were not well known, the amplitudes of each trace were normalized by each maximum amplitude. The numbers written by blue characters are cross-correlation coefficients between observed and synthesized envelopes at each station. The upper-right panel shows the stations used (blue diamonds) and the epicentre location (yellow star).

References

Aki, K., & Richards, P. (2002). *Quantitative Seismology* (2nd ed.). University Science Books. Retrieved from https://www.ldeo.columbia.edu/~richards/Aki_Richards.html

Amante, C., & Eakins, B. W. (2009). ETOPO1 1 arc-minute global relief model: Precedures, data sources and analysis. NOAA Technical Memorandum NESDIS NGDC-24. *NOAA Technical Memorandum NESDIS NGDC-24. National Geophysical Data Center, NOAA*, (March), 19. https://doi.org/10.7289/V5C8276M

Ando, M. (1975). Source mechanisms and tectonic significance of historical earthquakes along the Nankai trough, Japan. *Tectonophysics*, *27*(2), 119–140. https://doi.org/10.1016/0040-1951(75)90102-X

Annoura, S., Obara, K., & Maeda, T. (2016). Total energy of deep low-frequency tremor in the Nankai subduction zone, southwest Japan. *Geophysical Research Letters*, *43*(6), 2562–2567. https://doi.org/10.1002/2016GL067780

Annoura, S., Hashimoto, T., Kamaya, N., & Katsumata, A. (2017). Shallow episodic tremor near the Nankai Trough axis off southeast Mie prefecture, Japan. *Geophysical Research Letters*, *44*(8), 3564–3571. https://doi.org/10.1002/2017GL073006

Araki, E., Saffer, D. M., Kopf, A. J., Wallace, L. M., Kimura, T., Machida, Y., et al. (2017). Recurring and triggered slow-slip events near the trench at the Nankai Trough subduction megathrust. *Science*, *356*(6343), 1157–1160. https://doi.org/10.1126/science.aan3120

Battaglia, J., & Aki, K. (2003). Location of seismic events and eruptive fissures on the Piton de la Fournaise volcano using seismic amplitudes. *Journal of Geophysical Research*, *108*(B8), 2364. https://doi.org/10.1029/2002JB002193

Carcolé, E., & Sato, H. (2010). Spatial distribution of scattering loss and intrinsic absorption of short-period S waves in the lithosphere of Japan on the basis of the Multiple Lapse Time Window Analysis of Hi-net data. *Geophysical Journal International*, *180*(1), 268–290. https://doi.org/10.1111/j.1365-246X.2009.04394.x

Chaput, J., Campillo, M., Aster, R. C., Roux, P., Kyle, P. R., Knox, H., & Czoski, P. (2015). Multiple scattering from icequakes at Erebus volcano, Antarctica: Implications for imaging at glaciated volcanoes. *Journal of Geophysical Research: Solid Earth*, *120*(2), 1129–1141. https://doi.org/10.1002/2014JB011278

Ekström, G., Nettles, M., & Dziewoński, A. M. (2012). The global CMT project 2004-2010: Centroid-moment tensors for 13,017 earthquakes. *Physics of the Earth and Planetary Interiors*, *200–201*, 1–9. https://doi.org/10.1016/j.pepi.2012.04.002

Ellsworth, W. L., & Bulut, F. (2018). Nucleation of the 1999 Izmit earthquake by a triggered cascade of foreshocks. *Nature Geoscience*, *11*(7), 531–535. https://doi.org/10.1038/s41561-018-0145-1

Fletcher, J. B., & McGarr, A. (2011). Moments, magnitudes, and radiated energies of non-

volcanic tremor near Cholame, CA, from ground motion spectra at UPSAR. *Geophysical Research Letters*, *38*(16), n/a-n/a. https://doi.org/10.1029/2011GL048636

Furumura, T., & Kennett, B. L. N. (2005). Subduction zone guided waves and the heterogeneity structure of the subducted plate: Intensity anomalies in northern Japan. *Journal of Geophysical Research*, *110*(B10), B10302. https://doi.org/10.1029/2004JB003486

Furumura, Takashi, & Kennett, B. L. N. (2018). Regional Distance PL Phase in the Crustal Waveguide-An Analog to the Teleseismic W Phase in the Upper-Mantle Waveguide. *Journal of Geophysical Research: Solid Earth*, *123*(5), 4007–4024. https://doi.org/10.1029/2018JB015717

Ghosh, A., Vidale, J. E., Sweet, J. R., Creager, K. C., & Wech, A. G. (2009). Tremor patches in Cascadia revealed by seismic array analysis. *Geophysical Research Letters*, *36*(17), L17316. https://doi.org/10.1029/2009GL039080

Gomberg, J. (2018). Cascadia Onshore-Offshore Site Response, Submarine Sediment Mobilization, and Earthquake Recurrence. *Journal of Geophysical Research: Solid Earth*, *123*(2), 1381–1404. https://doi.org/10.1002/2017JB014985

Gomberg, J., Wech, A., Creager, K., Obara, K., & Agnew, D. (2016). Reconsidering earthquake scaling. *Geophysical Research Letters*, *43*(12), 6243–6251. https://doi.org/10.1002/2016GL069967

Gusev, A. A., & Pavlov, V. M. (1991). Deconvolution of squared velocity waveform as applied to the study of a noncoherent short-period radiator in the earthquake source. *Pure and Applied Geophysics*, *136*(2–3), 235–244. https://doi.org/10.1007/BF00876375

Haney, M. M., & Tsai, V. C. (2017). Perturbational and nonperturbational inversion of Rayleigh-wave velocities. *GEOPHYSICS*, *82*(3), F15–F28. https://doi.org/10.1190/geo2016-0397.1

Hawthorne, J. C., Thomas, A. M., & Ampuero, J.-P. (2019). The rupture extent of low frequency earthquakes near Parkfield, CA. *Geophysical Journal International*, *216*(1), 621–639. https://doi.org/10.1093/gji/ggy429

Hejrani, B., Tkalčić, H., & Fichtner, A. (2017). Centroid moment tensor catalogue using a 3-D continental scale Earth model: Application to earthquakes in Papua New Guinea and the Solomon Islands. *Journal of Geophysical Research: Solid Earth*, *122*(7), 5517–5543. https://doi.org/10.1002/2017JB014230

Helffrich, G., Wookey, J., & Bastow, I. (2013). *The Seismic Analysis Code*. Cambridge: Cambridge University Press. https://doi.org/10.1017/CBO9781139547260

Ide, S. (2010). Striations, duration, migration and tidal response in deep tremor. *Nature*, *466*(7304), 356–359. https://doi.org/10.1038/nature09251

Ide, S., & Maury, J. (2018). Seismic Moment, Seismic Energy, and Source Duration of Slow Earthquakes: Application of Brownian slow earthquake model to three major subduction

zones. *Geophysical Research Letters*, *45*(7), 3059–3067. https://doi.org/10.1002/2018GL077461

Ide, S., & Yabe, S. (2014). Universality of slow earthquakes in the very low frequency band. *Geophysical Research Letters*, *41*(8), 2786–2793. https://doi.org/10.1002/2014GL059712

Ide, S., Beroza, G. C., Prejean, S. G., & Ellsworth, W. L. (2003). Apparent break in earthquake scaling due to path and site effects on deep borehole recordings. *Journal of Geophysical Research: Solid Earth*, *108*(B5). https://doi.org/10.1029/2001JB001617

Ide, S., Imanishi, K., Yoshida, Y., Beroza, G. C., & Shelly, D. R. (2008). Bridging the gap between seismically and geodetically detected slow earthquakes. *Geophysical Research Letters*, *35*(10), 2–7. https://doi.org/10.1029/2008GL034014

Imperatori, W., & Mai, P. M. (2013). Broad-band near-field ground motion simulations in 3-dimensional scattering media. *Geophysical Journal International*, *192*(2), 725–744. https://doi.org/10.1093/gji/ggs041

Imperatori, W., & Mai, P. M. (2015). The role of topography and lateral velocity heterogeneities on near-source scattering and ground-motion variability. *Geophysical Journal International*, *202*(3), 2163–2181. https://doi.org/10.1093/gji/ggv281

Iwaki, A., Maeda, T., Morikawa, N., Takemura, S., & Fujiwara, H. (2018). Effects of random 3D upper crustal heterogeneity on long-period (≥ 1 s) ground-motion simulations. *Earth, Planets and Space*, *70*(1), 156. https://doi.org/10.1186/s40623-018-0930-5

Kanamori, H., & Rivera, L. (2008). Source inversion of W phase: Speeding up seismic tsunami warning. *Geophysical Journal International*, *175*(1), 222–238. https://doi.org/10.1111/j.1365-246X.2008.03887.x

Kaneko, Y., Ito, Y., Chow, B., Wallace, L. M., Tape, C., Grapenthin, R., et al. (2019). Ultra-long Duration of Seismic Ground Motion Arising From a Thick, Low-Velocity Sedimentary Wedge. *Journal of Geophysical Research: Solid Earth*, *124*(10), 10347–10359. https://doi.org/10.1029/2019JB017795

Kano, M., Aso, N., Matsuzawa, T., Ide, S., Annoura, S., Arai, R., et al. (2018). Development of a Slow Earthquake Database. *Seismological Research Letters*, *89*(4), 1566–1575. https://doi.org/10.1785/0220180021

Kao, H., Wang, K., Dragert, H., Kao, J. Y., & Rogers, G. (2010). Estimating seismic moment magnitude (M w) of tremor bursts in northern Cascadia: Implications for the “seismic efficiency” of episodic tremor and slip. *Geophysical Research Letters*, *37*(19), n/a-n/a. https://doi.org/10.1029/2010GL044927

Kato, A., Obara, K., Igarashi, T., Tsuruoka, H., Nakagawa, S., & Hirata, N. (2012). Propagation of slow slip leading up to the 2011 Mw9.0 Tohoku-Oki earthquake. *Science*, *335*(6069), 705–708. https://doi.org/10.1126/science.1215141

Koketsu, K., Miyake, H., & Suzuki, H. (2012). Japan Integrated Velocity Structure Model

Version 1. *Proceedings of the 15th World Conference on Earthquake Engineering*, 1–4. Retrieved from http://www.iitk.ac.in/nicee/wcee/article/WCEE2012_1773.pdf

Kubo, H., Nakamura, T., Suzuki, W., Kimura, T., Kunugi, T., Takahashi, N., & Aoi, S. (2018). Site Amplification Characteristics at Nankai Seafloor Observation Network, DONET1, Japan, Evaluated Using Spectral Inversion. *Bulletin of the Seismological Society of America*, *XX*(Xx), 1–9. https://doi.org/10.1785/0120170254

Kumagai, H., Lacson, R., Maeda, Y., Figueroa, M. S., Yamashina, T., Ruiz, M., et al. (2013). Source amplitudes of volcano-seismic signals determined by the amplitude source location method as a quantitative measure of event size. *Journal of Volcanology and Geothermal Research*, *257*, 57–71. https://doi.org/10.1016/j.jvolgeores.2013.03.002

Kurokawa, A., Takeo, M., & Kurita, K. (2016). Two types of volcanic tremor changed with eruption style during 1986 Izu-Oshima eruption. *Journal of Geophysical Research: Solid Earth*, *121*(4), 2727–2736. https://doi.org/10.1002/2015JB012500

Maeda, T., & Obara, K. (2009). Spatiotemporal distribution of seismic energy radiation from low-frequency tremor in western Shikoku, Japan. *Journal of Geophysical Research: Solid Earth*, *114*(10). https://doi.org/10.1029/2008JB006043

Maeda, T., Takemura, S., & Furumura, T. (2017). OpenSWPC: an open-source integrated parallel simulation code for modeling seismic wave propagation in 3D heterogeneous viscoelastic media. *Earth, Planets and Space*, *69*(1), 102. https://doi.org/10.1186/s40623-017-0687-2

Margerin, L. (2005). Introduction to radiative transfer of seismic waves. *Geophysical Monograph Series*, *157*(January 2005), 229–252. https://doi.org/10.1029/157GM14

Morioka, H., Kumagai, H., & Maeda, T. (2017). Theoretical basis of the amplitude source location method for volcano-seismic signals. *Journal of Geophysical Research: Solid Earth*, *122*(8), 6538–6551. https://doi.org/10.1002/2017JB013997

Muyzert, E. (2007). Seabed property estimation from ambient-noise recordings: Part I — Compliance and Scholte wave phase-velocity measurements. *GEOPHYSICS*, *72*(2), U21–U26. https://doi.org/10.1190/1.2435587

Nakahara, H. (2008). Chapter 15 Seismogram Envelope Inversion for High-Frequency Seismic Energy Radiation from Moderate-to-Large Earthquakes. In *Advances in Geophysics* (Vol. 50, pp. 401–426). https://doi.org/10.1016/S0065-2687(08)00015-0

Nakahara, H. (2013). Envelope inversion analysis for high-frequency seismic energy radiation from the 2011 Mw 9.0 Off the Pacific Coast of Tohoku earthquake. *Bulletin of the Seismological Society of America*, *103*(2 B), 1348–1359. https://doi.org/10.1785/0120120155

Nakamura, T., Takenaka, H., Okamoto, T., Ohori, M., & Tsuboi, S. (2015). Long-period ocean-bottom motions in the source areas of large subduction earthquakes. *Scientific Reports*, *5*, 1–2. https://doi.org/10.1038/srep16648

Nakano, M., Kumagai, H., & Inoue, H. (2008). Waveform inversion in the frequency domain for the simultaneous determination of earthquake source mechanism and moment function. *Geophysical Journal International*, *173*(3), 1000–1011. https://doi.org/10.1111/j.1365-246X.2008.03783.x

Nakano, M., Tonegawa, T., & Kaneda, Y. (2012). Orientations of DONET seismometers estimated from seismic waveforms. *JAMSTEC Report of Research and Development*, *15*(0), 77–89. https://doi.org/10.5918/jamstecr.15.77

Nakano, M., Nakamura, T., & Kaneda, Y. (2015). Hypocenters in the nankai trough determined by using data from both ocean-bottom and land seismic networks and a 3D velocity structure model: Implications for seismotectonic activity. *Bulletin of the Seismological Society of America*, *105*(3), 1594–1605. https://doi.org/10.1785/0120140309

Nakano, M., Hori, T., Araki, E., Kodaira, S., & Ide, S. (2018). Shallow very-low-frequency earthquakes accompany slow slip events in the Nankai subduction zone. *Nature Communications*, *9*(1), 984. https://doi.org/10.1038/s41467-018-03431-5

Nakano, M., Hyodo, M., Nakanishi, A., Yamashita, M., Hori, T., Kamiya, S., et al. (2018). The 2016 Mw 5.9 earthquake off the southeastern coast of Mie Prefecture as an indicator of preparatory processes of the next Nankai Trough megathrust earthquake. *Progress in Earth and Planetary Science*, *5*(1), 30. https://doi.org/10.1186/s40645-018-0188-3

Nakano, M., Yabe, S., Sugioka, H., Shinohara, M., & Ide, S. (2019). Event Size Distribution of Shallow Tectonic Tremor in the Nankai Trough. *Geophysical Research Letters*, *46*(11), 5828–5836. https://doi.org/10.1029/2019GL083029

National Research Institute for Earth Science and Disaster Resilience. (2019a). NIED DONET. https://doi.org/10.17598/NIED.0008

National Research Institute for Earth Science and Disaster Resilience. (2019b). NIED F-net. https://doi.org/10.17598/NIED.0005

National Research Institute for Earth Science and Disaster Resilience. (2019c). NIED S-net. https://doi.org/10.17598/NIED.0007

Nishida, K. (2017). Ambient seismic wave field. *Proceedings of the Japan Academy, Series B*, *93*(7), 423–448. https://doi.org/10.2183/pjab.93.026

Nishikawa, T., Matsuzawa, T., Ohta, K., Uchida, N., Nishimura, T., & Ide, S. (2019). The slow earthquake spectrum in the Japan Trench illuminated by the S-net seafloor observatories. *Science*, *365*(August), 808–813. https://doi.org/10.1126/science.aax5618

Noguchi, S., Maeda, T., & Furumura, T. (2016). Ocean-influenced Rayleigh waves from outer-rise earthquakes and their effects on durations of long-period ground motion. *Geophysical Journal International*, *205*(2), 1099–1107. https://doi.org/10.1093/gji/ggw074

Obara, K., & Maeda, T. (2009). Reverse propagation of T waves from the Emperor seamount chain. *Geophysical Research Letters*, *36*(8), 1–5. https://doi.org/10.1029/2009GL037454

Okal, E. A. (2008). The generation of T waves by earthquakes (pp. 1–65). https://doi.org/10.1016/S0065-2687(07)49001-X

Peng, Z., & Zhao, P. (2009). Migration of early aftershocks following the 2004 Parkfield earthquake. *Nature Geoscience*, *2*(12), 877–881. https://doi.org/10.1038/ngeo697

Petukhin, A., Miyakoshi, K., Tsurugi, M., Kawase, H., & Kamae, K. (2016). Visualization of Green ' s function anomalies for megathrust source in Nankai Trough by reciprocity method. *Earth, Planets and Space*. https://doi.org/10.1186/s40623-016-0385-5

Petukhin, A. G., Nakahara, H., & Gusev, A. A. (2004). Inversion of the high-frequency source radiation of M6 . 8 Avachinsky Gulf , Kamchatka , earthquake using empirical and theoretical envelope Green functions, (1998), 921–925.

Poiata, N., Vilotte, J.-P., Bernard, P., Satriano, C., & Obara, K. (2018). Imaging different components of a tectonic tremor sequence in southwestern Japan using an automatic statistical detection and location method. *Geophysical Journal International*, (February). https://doi.org/10.1093/gji/ggy070/4898035

Przybilla, J., Wegler, U., & Korn, M. (2009). Estimation of crustal scattering parameters with elastic radiative transfer theory. *Geophysical Journal International*, *178*(2), 1105–1111. https://doi.org/10.1111/j.1365-246X.2009.04204.x

Saito, T., Sato, H., & Ohtake, M. (2002). Envelope broadening of spherically outgoing waves in three-dimensional random media having power law spectra. *Journal of Geophysical Research*, *107*(B5), 2089. https://doi.org/10.1029/2001JB000264

Saito, T., Sato, H., Ohtake, M., & Obara, K. (2005). Unified explanation of envelope broadening and maximum-amplitude decay high-frequency seismograms based on the envelope simulation using the Markov approximation: Forearc side of the volcanic front in northeastern Honshu, Japan. *Journal of Geophysical Research B: Solid Earth*, *110*(1), 1–18. https://doi.org/10.1029/2004JB003225

Sakai, S., Yamada, T., Shinohara, M., Hagiwara, H., Kanazawa, T., Obana, K., et al. (2005). Urgent aftershock observation of the 2004 off the Kii Peninsula earthquake using ocean bottom seismometers. *Earth Planets and Space*, *57*, 363–368. https://doi.org/10.1186/BF03352577

Sato, H., & Emoto, K. (2018). Synthesis of a Scalar Wavelet Intensity Propagating Through von Kármán-type Random Media: Radiative Transfer Theory Using the Born and Phase-Screen Approximations. *Geophysical Journal International*, 909–923. https://doi.org/10.1093/gji/ggy319

Sato, H., Fehler, M. C., & Maeda, T. (2012). Seismic Wave Propagation and Scattering in the Heterogeneous Earth : Second Edition. In *Seismic Wave Propagation and Scattering in the Heterogeneous Earth : Second Edition*. Berlin, Heidelberg: Springer Berlin

Heidelberg. https://doi.org/10.1007/978-3-642-23029-5_2

Sawazaki, K., & Enescu, B. (2014). Imaging the high-frequency energy radiation process of a main shock and its early aftershock sequence: The case of the 2008 Iwate-Miyagi Nairiku earthquake, Japan. *Journal of Geophysical Research: Solid Earth*, *119*(6), 4729–4746. https://doi.org/10.1002/2013JB010539

Shapiro, N. M., Campillo, M., Singh, S. K., & Pacheco, J. (1998). Seismic channel waves in the accretionary prism of the Middle America Trench. *Geophysical Research Letters*, *25*(1), 101–104. https://doi.org/10.1029/97GL03492

Shapiro, N. M., Olsen, K. B., & Singh, S. K. (2000). Wave-guide effects in subduction zones: Evidence from three-dimensional modeling. *Geophysical Research Letters*, *27*(3), 433–436. https://doi.org/10.1029/1999GL010982

Staudenmaier, N., Edwards, B., Tormann, T., Zechar, J. D., & Wiemer, S. (2016). Spatial distribution and energy release of nonvolcanic tremor at Parkfield, California. *Journal of Geophysical Research: Solid Earth*, *121*(12), 8833–8854. https://doi.org/10.1002/2016JB013283

Supino, M., Poiata, N., Festa, G., Vilotte, J. P., Satriano, C., & Obara, K. (2020). Self-similarity of low-frequency earthquakes. *Scientific Reports*, *10*(1), 1–9. https://doi.org/10.1038/s41598-020-63584-6

Takahashi, D. (2013). Implementation of Parallel 1-D FFT on GPU Clusters. In *2013 IEEE 16th International Conference on Computational Science and Engineering* (pp. 174–180). IEEE. https://doi.org/10.1109/CSE.2013.36

Takahashi, T., Sato, H., Nishimura, T., & Obara, K. (2007). Strong inhomogeneity beneath quaternary volcanoes revealed from the peak delay analysis of S-wave seismograms of microearthquakes in northeastern Japan. *Geophysical Journal International*, *168*(1), 90–99. https://doi.org/10.1111/j.1365-246X.2006.03197.x

Takahashi, T., Sato, H., Nishimura, T., & Obara, K. (2009). Tomographic inversion of the peak delay times to reveal random velocity fluctuations in the lithosphere: Method and application to northeastern Japan. *Geophysical Journal International*, *178*(3), 1437–1455. https://doi.org/10.1111/j.1365-246X.2009.04227.x

Takemura, S., & Yoshimoto, K. (2014). Strong seismic wave scattering in the low-velocity anomaly associated with subduction of oceanic plate. *Geophysical Journal International*, *197*(2), 1016–1032. https://doi.org/10.1093/gji/ggu031

Takemura, S., Furumura, T., & Saito, T. (2009). Distortion of the apparent S -wave radiation pattern in the high-frequency wavefield: Tottori-Ken Seibu, Japan, earthquake of 2000. *Geophysical Journal International*, *178*(2), 950–961. https://doi.org/10.1111/j.1365-246X.2009.04210.x

Takemura, S., Furumura, T., & Maeda, T. (2015). Scattering of high-frequency seismic waves caused by irregular surface topography and small-scale velocity inhomogeneity.

935 *Geophysical Journal International*, *201*(1), 459–474. https://doi.org/10.1093/gji/ggv038
936 Takemura, S., Kobayashi, M., & Yoshimoto, K. (2016). Prediction of maximum P- and S-
937 wave amplitude distributions incorporating frequency- and distance-dependent
938 characteristics of the observed apparent radiation patterns. *Earth, Planets and Space*,
939 *68*(1), 166. https://doi.org/10.1186/s40623-016-0544-8
940 Takemura, S., Kobayashi, M., & Yoshimoto, K. (2017). High-frequency seismic wave
941 propagation within the heterogeneous crust: effects of seismic scattering and intrinsic
942 attenuation on ground motion modelling. *Geophysical Journal International*, *210*(3),
943 1806–1822. https://doi.org/10.1093/gji/ggx269
944 Takemura, S., Kubo, H., Tonegawa, T., Saito, T., & Shiomi, K. (2019). Modeling of Long-
945 Period Ground Motions in the Nankai Subduction Zone: Model Simulation Using the
946 Accretionary Prism Derived from Oceanfloor Local S-Wave Velocity Structures. *Pure*
947 *and Applied Geophysics*, *176*(2), 627–647. https://doi.org/10.1007/s00024-018-2013-8
948 Takemura, S., Yoshimoto, K., & Tonegawa, T. (2015). Scattering of trapped P and S waves
949 in the hydrated subducting crust of the Philippine Sea plate at shallow depths beneath
950 the Kanto region, Japan. *Geophysical Journal International*, *203*(3), 2261–2276.
951 https://doi.org/10.1093/gji/ggv423
952 Takemura, S., Shiomi, K., Kimura, T., & Saito, T. (2016). Systematic difference between
953 first-motion and waveform-inversion solutions for shallow offshore earthquakes due to a
954 low-angle dipping slab. *Earth, Planets and Space*, *68*(1), 149.
955 https://doi.org/10.1186/s40623-016-0527-9
956 Takemura, S., Matsuzawa, T., Noda, A., Tonegawa, T., Asano, Y., Kimura, T., & Shiomi, K.
957 (2019). Structural Characteristics of the Nankai Trough Shallow Plate Boundary
958 Inferred From Shallow Very Low Frequency Earthquakes. *Geophysical Research*
959 *Letters*, *46*(8), 4192–4201. https://doi.org/10.1029/2019GL082448
960 Takemura, S., Okuwaki, R., Kubota, T., Shiomi, K., Kimura, T., & Noda, A. (2020). Centroid
961 moment tensor inversions of offshore earthquakes using a three-dimensional velocity
962 structure model: slip distributions on the plate boundary along the Nankai Trough.
963 *Geophysical Journal International*, *222*(2), 1109–1125.
964 https://doi.org/10.1093/gji/ggaa238
965 Takeo, A., Forsyth, D. W., Weeraratne, D. S., & Nishida, K. (2014). Estimation of azimuthal
966 anisotropy in the NW Pacific from seismic ambient noise in seafloor records.
967 *Geophysical Journal International*, *199*(1), 11–22. https://doi.org/10.1093/gji/ggu240
968 Tamaribuchi, K., Kobayashi, A., Nishimiya, T., Hirose, F., & Annoura, S. (2019).
969 Characteristics of shallow low-frequency earthquakes off the Kii Peninsula, Japan, in
970 2004 revealed by ocean bottom seismometers. *Geophysical Research Letters*,
971 2019GL085158. https://doi.org/10.1029/2019GL085158
972 Tanaka, S., Matsuzawa, T., & Asano, Y. (2019). Shallow Low-Frequency Tremor in the

973 Northern Japan Trench Subduction Zone. *Geophysical Research Letters*, *46*(10), 5217–
974 5224. https://doi.org/10.1029/2019GL082817
975 Thomas, A. M., Beroza, G. C., & Shelly, D. R. (2016). Constraints on the source parameters
976 of low-frequency earthquakes on the San Andreas Fault. *Geophysical Research Letters*,
977 *43*(4), 1464–1471. https://doi.org/10.1002/2015GL067173
978 Toh, A., Obana, K., & Araki, E. (2018). Distribution of very low frequency earthquakes in
979 the Nankai accretionary prism influenced by a subducting-ridge. *Earth and Planetary*
980 *Science Letters*, *482*(March 2011), 342–356. https://doi.org/10.1016/j.epsl.2017.10.062
981 Tonegawa, T., Fukao, Y., Takahashi, T., Obana, K., Kodaira, S., & Kaneda, Y. (2015).
982 Ambient seafloor noise excited by earthquakes in the Nankai subduction zone. *Nature*
983 *Communications*, *6*, 1–7. https://doi.org/10.1038/ncomms7132
984 Tonegawa, T., Fukao, Y., Fujie, G., Takemura, S., Takahashi, T., & Kodaira, S. (2015).
985 Geographical distribution of shear wave anisotropy within marine sediments in the
986 northwestern Pacific. *Progress in Earth and Planetary Science*, *2*(1), 27.
987 https://doi.org/10.1186/s40645-015-0057-2
988 Tonegawa, T., Araki, E., Kimura, T., Nakamura, T., Nakano, M., & Suzuki, K. (2017).
989 Sporadic low-velocity volumes spatially correlate with shallow very low frequency
990 earthquake clusters. *Nature Communications*, *8*(1), 2048.
991 https://doi.org/10.1038/s41467-017-02276-8
992 Tripathi, J. N., Sato, H., & Yamamoto, M. (2010). Envelope broadening characteristics of
993 crustal earthquakes in northeastern Honshu, Japan. *Geophysical Journal International*,
994 *182*(2), 988–1000. https://doi.org/10.1111/j.1365-246X.2010.04657.x
995 Uchide, T., & Ide, S. (2010). Scaling of earthquake rupture growth in the Parkfield area: Self-
996 similar growth and suppression by the finite seismogenic layer. *Journal of Geophysical*
997 *Research: Solid Earth*, *115*(11), 1–15. https://doi.org/10.1029/2009JB007122
998 Volk, O., Shani-kadmiel, S., Gvirtzman, Z., & Tsesarsky, M. (2017). 3D Effects of
999 Sedimentary Wedges and Subsurface Canyons : Ground-Motion Amplification in the
1000 Israeli Coastal Plain, *107*(3). https://doi.org/10.1785/0120160349
1001 Wallace, L. M., Araki, E., Saffer, D., Wang, X., Roesner, A., Kopf, A., et al. (2016). Near-
1002 field observations of an offshore M w 6.0 earthquake from an integrated seafloor and
1003 subseafloor monitoring network at the Nankai Trough, southwest Japan. *Journal of*
1004 *Geophysical Research: Solid Earth*, *121*(11), 8338–8351.
1005 https://doi.org/10.1002/2016JB013417
1006 Wang, X., & Zhan, Z. (2020). Moving from 1-D to 3-D velocity model: automated
1007 waveform-based earthquake moment tensor inversion in the Los Angeles region.
1008 *Geophysical Journal International*, *220*(1), 218–234. https://doi.org/10.1093/gji/ggz435
1009 Wegler, U., Korn, M., & Przybilla, J. (2006). Modeling Full Seismogram Envelopes Using
1010 Radiative Transfer Theory with Born Scattering Coefficients. *Pure and Applied*

Geophysics, *163*(2–3), 503–531. https://doi.org/10.1007/s00024-005-0027-5

Wessel, P., Smith, W. H. F., Scharroo, R., Luis, J., & Wobbe, F. (2013). Generic mapping tools: Improved version released. *Eos*, *94*(45), 409–410. https://doi.org/10.1002/2013EO450001

Yabe, S., & Ide, S. (2014). Spatial distribution of seismic energy rate of tectonic tremors in subduction zones. *Journal of Geophysical Research: Solid Earth*, *119*(11), 8171–8185. https://doi.org/10.1002/2014JB011383

Yabe, S., Tonegawa, T., & Nakano, M. (2019). Scaled Energy Estimation for Shallow Slow Earthquakes. *Journal of Geophysical Research: Solid Earth*, *124*(2), 1507–1519. https://doi.org/10.1029/2018JB016815

Yoshimoto, K., Takemura, S., & Kobayashi, M. (2015). Application of scattering theory to P-wave amplitude fluctuations in the crust. *Earth, Planets and Space*, *67*(1), 199. https://doi.org/10.1186/s40623-015-0366-0

Zhang, W., & Shen, Y. (2010). Unsplit complex frequency-shifted PML implementation using auxiliary differential equations for seismic wave modeling. *GEOPHYSICS*, *75*(4), T141–T154. https://doi.org/10.1190/1.3463431

Supporting information:
Modelling high-frequency seismograms at ocean bottom seismometers: effects of heterogeneous structures on source parameter estimation of small offshore earthquakes and shallow low-frequency tremors

Authors

Shunsuke TAKEMURA[1*], Suguru YABE[2], Kentaro EMOTO[3]

[1]Earthquake Research Institute, the University of Tokyo, 1-1-1 Yayoi, Bunkyo-ku, Tokyo, 113-0032, Japan

[2]Geological Survey of Japan, National Institute of Advanced Industrial Science and Technology, Tsukuba Central 7, 1-1-1 Higashi, Tsukuba, Ibaraki, 305-8567, Japan

[3]Geophysics, Graduate School of Science, Tohoku University, 6-3, Aramaki-aza-aoba, Aoba-ku, Sendai, 980-8578, Japan

Text S1

The 3D model used in the simulations was basically constructed from the Japan Integrated Velocity Structure Model (JIVSM) (Koketsu et al., 2012; Table 1 and Figure S1b). Because the accretionary prism of the JIVSM is modelled by a V_S = 1 km/s constant layer and is too simple for realistic ground motion simulation, we introduced estimations of 1D *S*-wave velocity structures beneath DONET stations by Tonegawa *et al.* (2017). We converted the depth-varying velocity structure model of Tonegawa *et al.* (2017) to a 5-layer model beneath each DONET station. The physical parameters of each layer are listed in Table 1 of the main text. Thicknesses of each layer were determined by fitting the depth-average *S*-wave velocities derived by Tonegawa *et al.* (2017). For example, if the depth-average V_S of Tonegawa *et al.* (2017) become the V_S of layer 1 at a certain depth, this depth is considered as the bottom of layer 1. After obtaining the bottom depths of layers 1–4 beneath DONET stations, the bottom depths of each station were interpolated and extrapolated via the '*Surface*' gridding algorithm in Generic Mapping Tools software (GMT; Wessel *et al.* 2013). Interpolation and extrapolation were only applied within the region of the accretionary prism (Figure S1). In other words, the JIVSM onshore and outer-rise sedimentary structures, and structures beneath bedrock, were fixed.

This construction method was basically the same as in Takemura, Kubo, *et al.* (2019). However, in the present model, a layered structure was employed rather than a depth velocity-gradient function. The simulation results of both the smooth-gradient and layered models were

almost the same (Figures S2–S4).

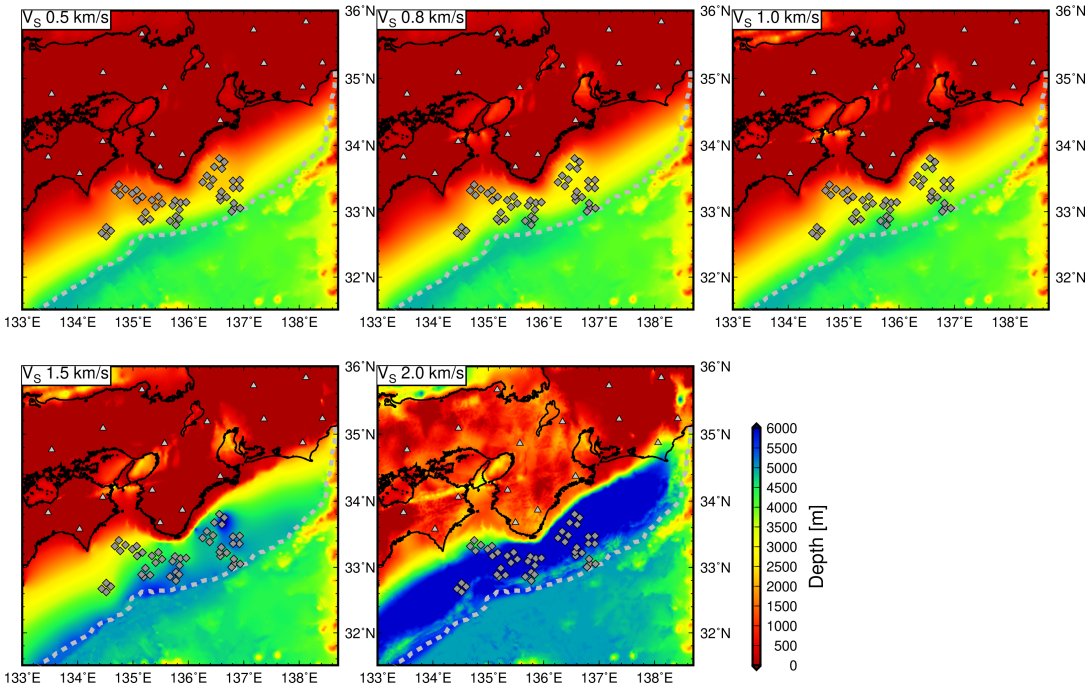

Figure S1a. The 3D layered structure of the accretionary prism. Background colours represent depths of the bottom of each layer (see Table 1). The bottom of layer with V_S of 2. 0 km/s is corresponding to the bedrock depths of the JIVSM (Koketsu et al., 2012).

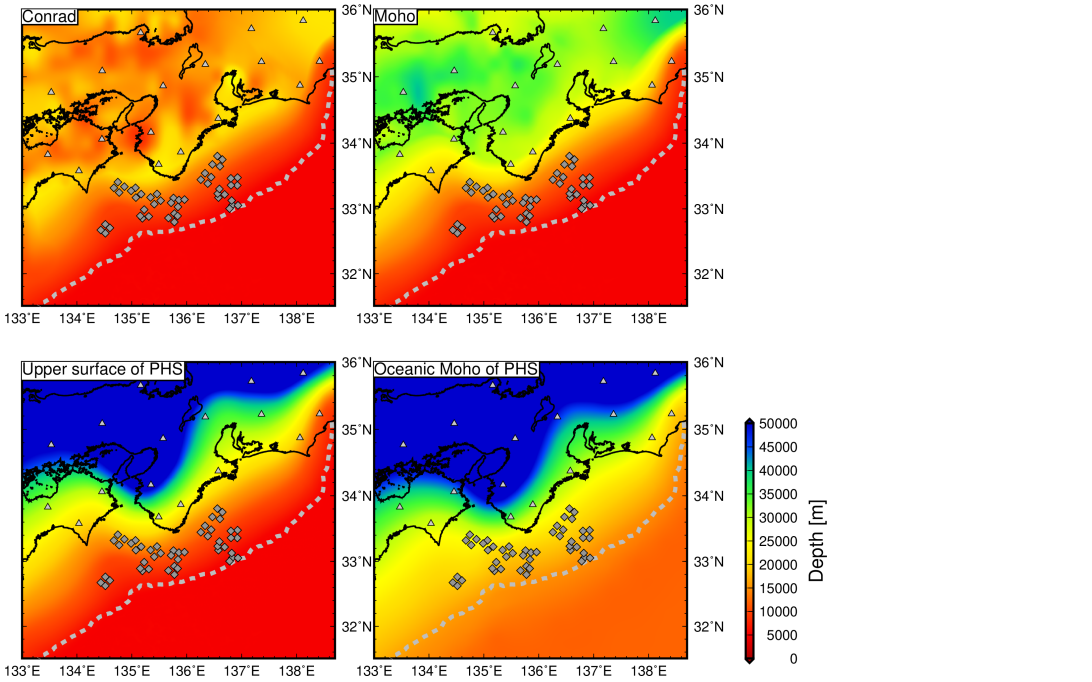

Figure S1b. Spatial variations of depths for Conrad, Moho, upper surface and oceanic Moho of the Philippine Sea plate in the assumed model, JIVSM (Koketsu et al., 2012).

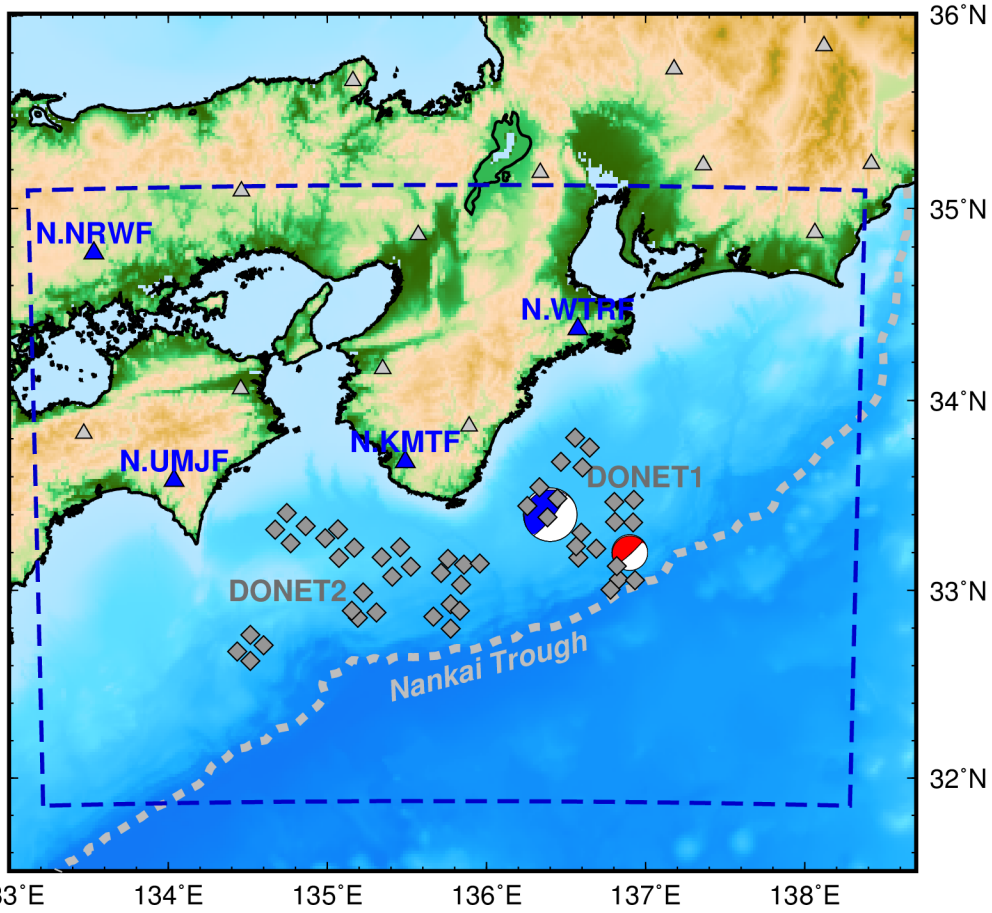

Figure S2. Map for validation of simulations. The dashed-blue rectangle represents the horizontal coverage of the calculation region, which was discretised at intervals of 0.2 km in horizontal directions and 0.1 km in the vertical direction. Simulations were conducted using the computer system at the Earthquake and Volcano Information Center, Earthquake Research Institute, University of Tokyo. The blue and red focal spheres are CMT solutions of the 2016 *Mw* 5.9 earthquake southeast off Kii Peninsula, Japan (Takemura et al., 2020), and a shallow very low-frequency earthquake on 10 April 2016 (Takemura et al., 2018, 2019), respectively. The triangles and diamonds represent F-net and DONET stations, respectively.

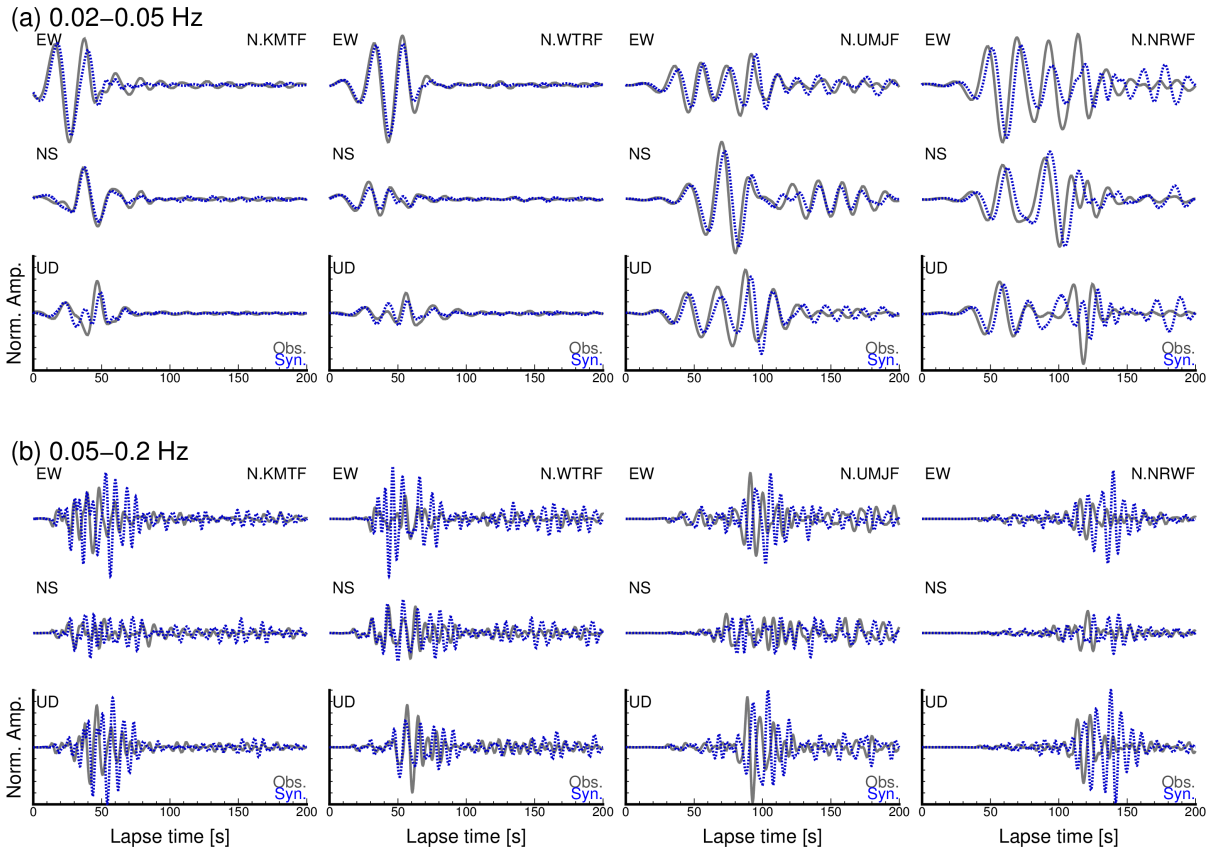

Figure S3. Simulation of the 2016 *Mw* 5.9 earthquake southeast off Kii Peninsula, Japan (Shunsuke Takemura et al., 2020): (a) 0.02–0.05 Hz, (b) 0.05–0.2 Hz. Seismic wave propagation in our model was evaluated via OpenSWPC software (Maeda et al., 2017). The simulation model covered the area within the blue rectangle shown in Figure S1, which was discretised by grid intervals of 0.2 km in horizontal directions and 0.1 km in the vertical direction. Observed and synthetic seismograms at F-net stations are represented by grey and blue dotted lines, respectively. Amplitudes at each station were normalized by the maximum amplitude of six-component filtered seismograms.

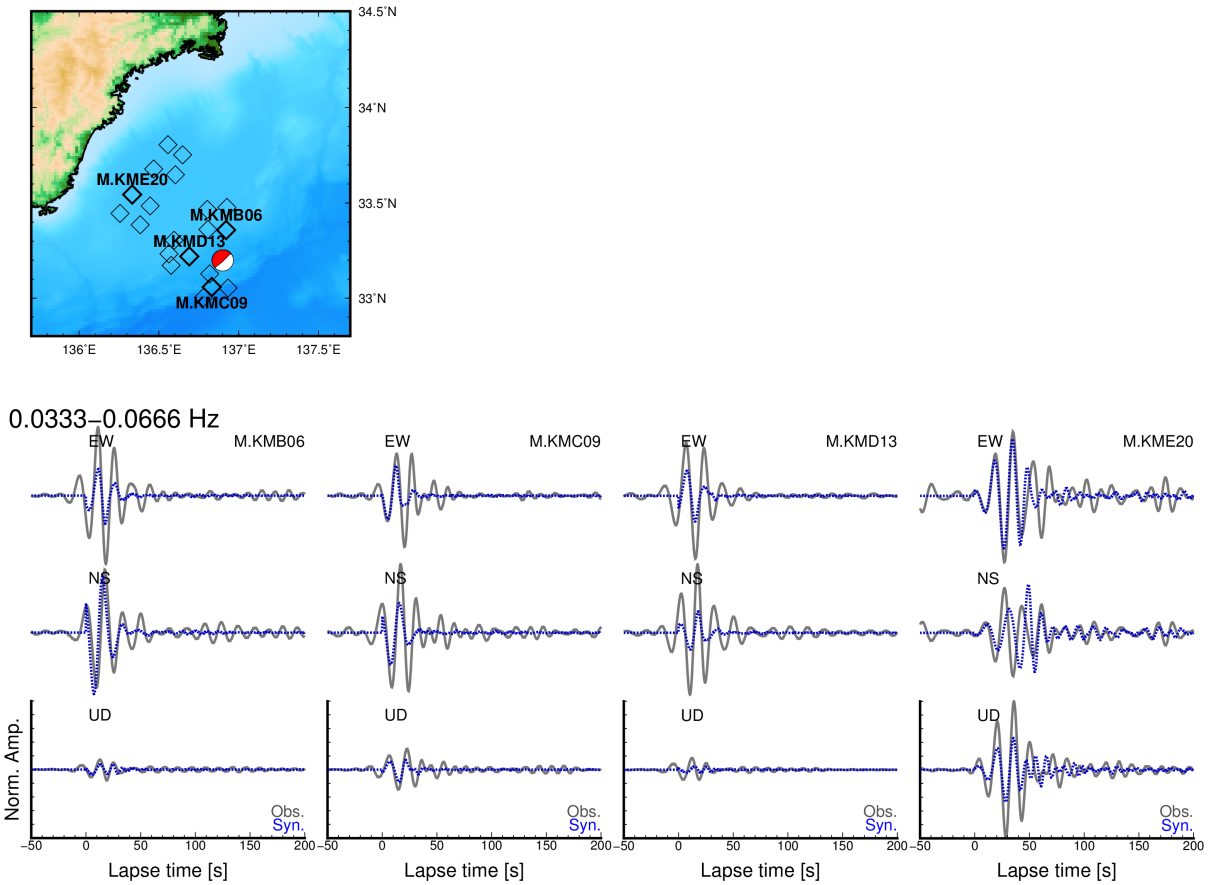

Figure S4. Simulation result of a shallow very low-frequency earthquake on 10 April 2016 (S. Takemura et al., 2018; Shunsuke Takemura et al., 2019). Observed and synthetic seismograms at DONET stations are represented by grey and blue dotted lines, respectively. Amplitudes at each station were normalized by the maximum amplitude of six-component filtered seismograms. Locations of stations and the source are shown in the upper-left panel. The simulation model and settings are similar to those in Figure S2.

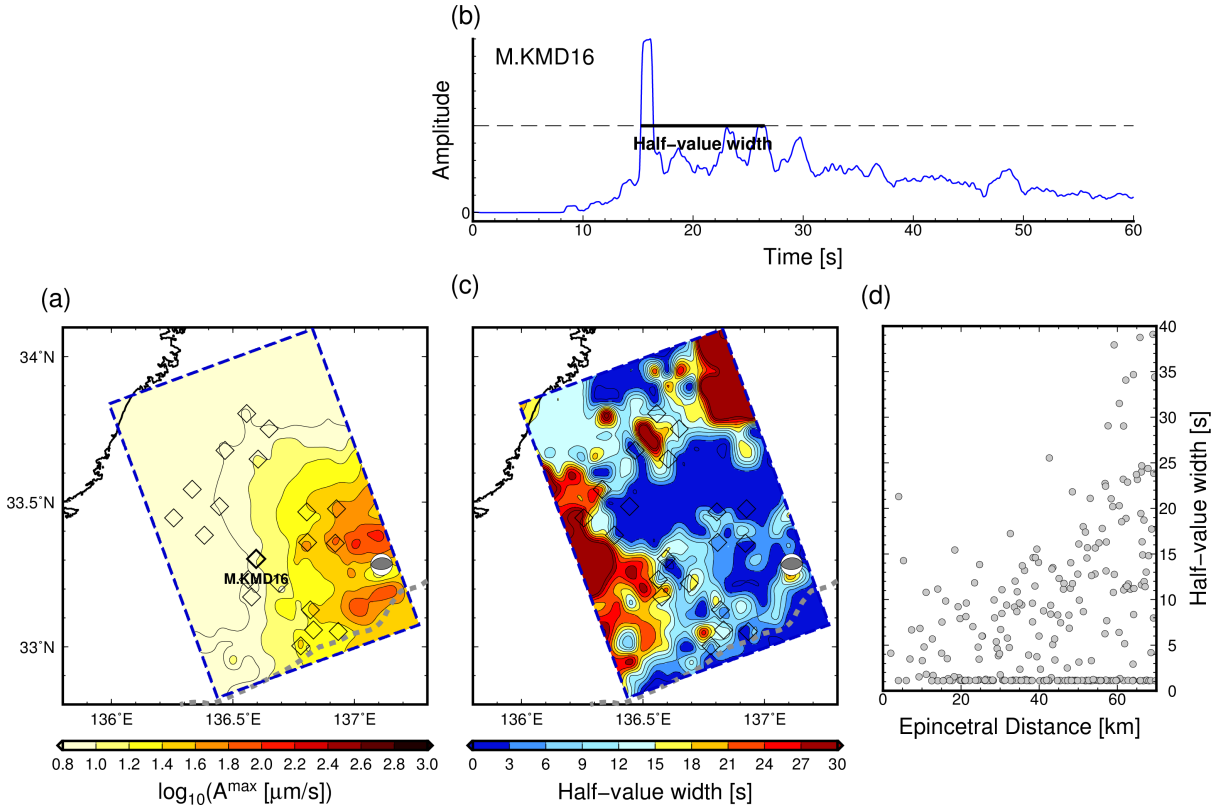

Figure S5. Spatial variations of maximum RMS amplitudes and half-value widths of simulated RMS envelopes for an intraslab earthquake: (a) Maximum RMS amplitude distribution, (b) example half-value width estimations, (c) half-value width distribution, and (d) half-value widths as a function of epicentral distance. An example in (b) is an RMS envelope at M.MRD16 (location shown in (a)).

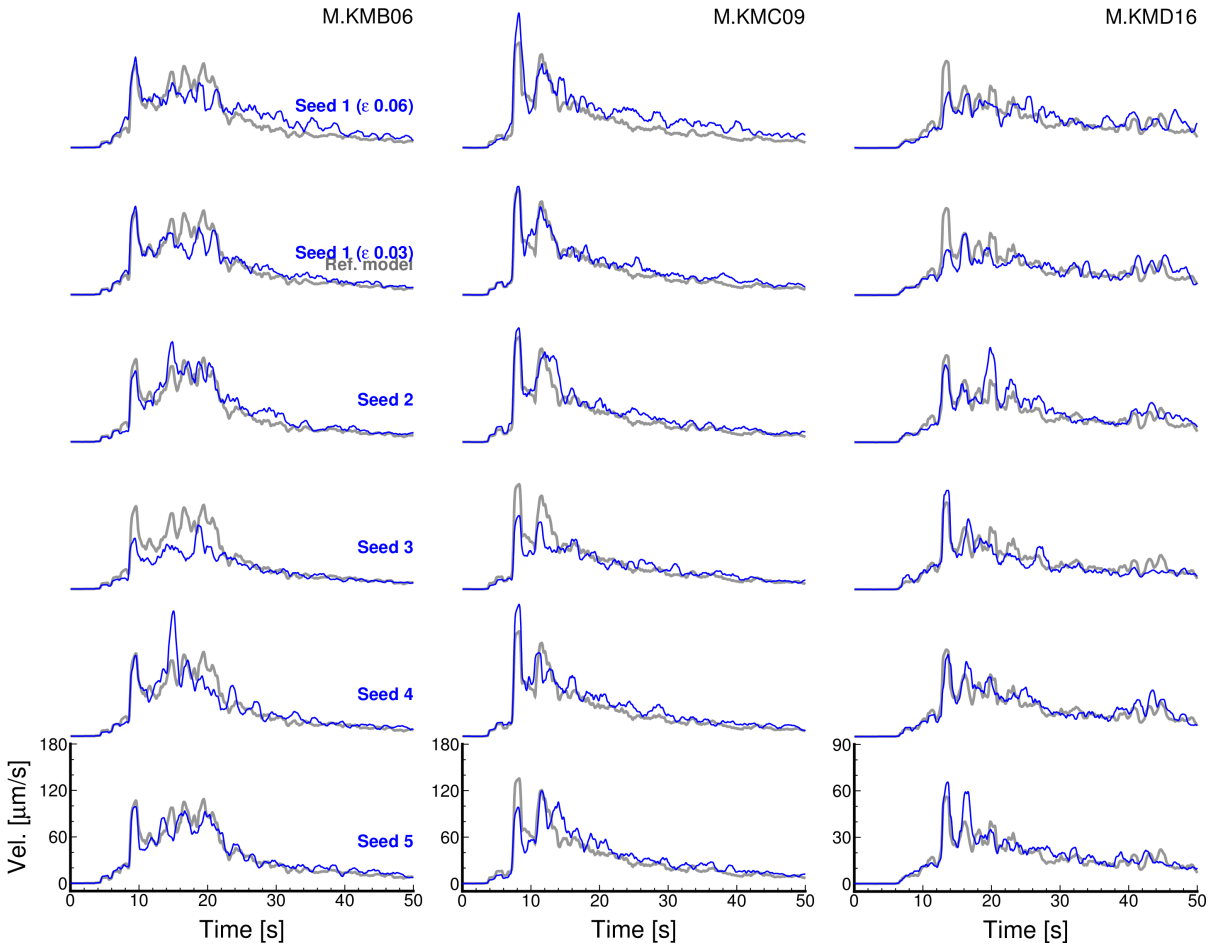

Figure S6. Comparisons of simulated RMS envelopes with different small-scale random velocity heterogeneity models. The PSDF type is an exponential type, and the parameters for small-scale random velocity heterogeneity models within the crust and accretionary prism are correlation length of a = 1 km and RMS values of ε = 0.03, 0.06. The models with a = 1 km and ε = 0.03 were conducted using different random seeds (numbered 1–5). Details of small-scale velocity heterogeneity models are described in Table 3. Locations of DONET stations are shown in Figure 8.

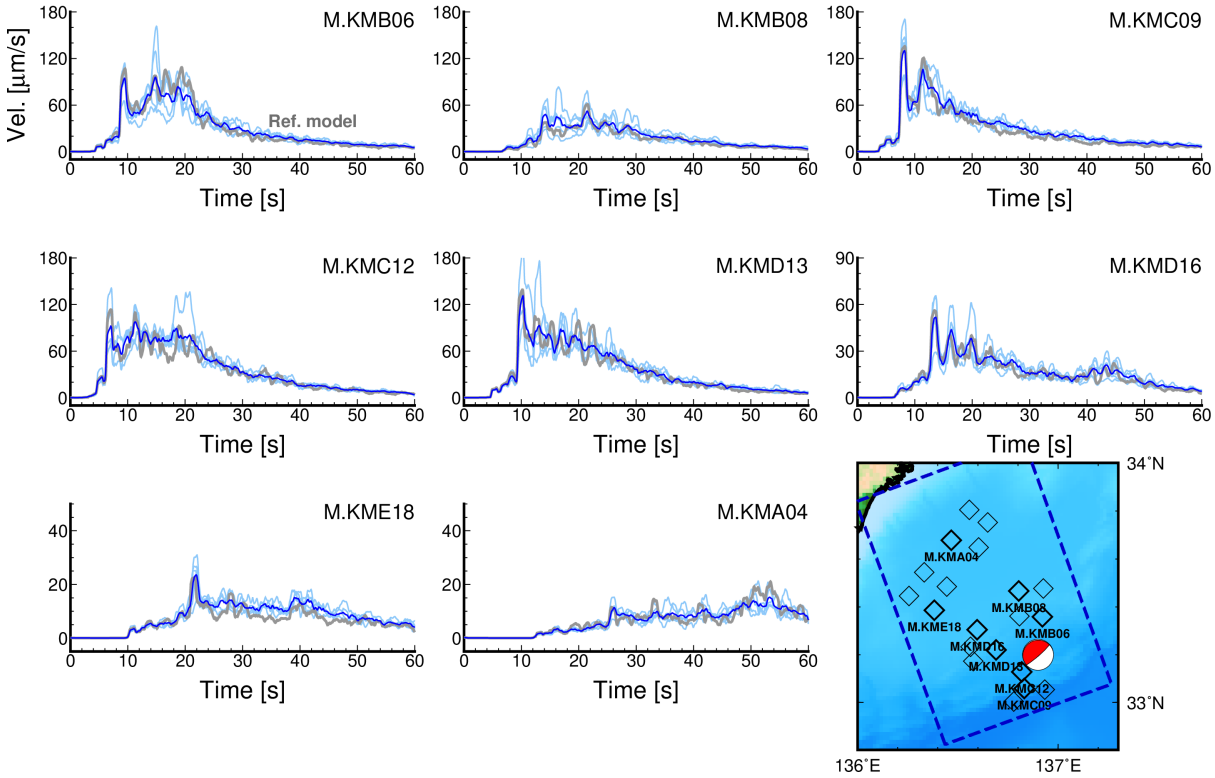

Figure S7. Comparisons between simulated envelopes with/without small-scale velocity heterogeneities. Grey lines are envelopes from the reference model (without small-scale velocity heterogeneities). Blue and light blue lines are stacked and individual envelopes in the model with small-scale velocity heterogeneities. Details of small-scale velocity heterogeneity models are described in Table 3.

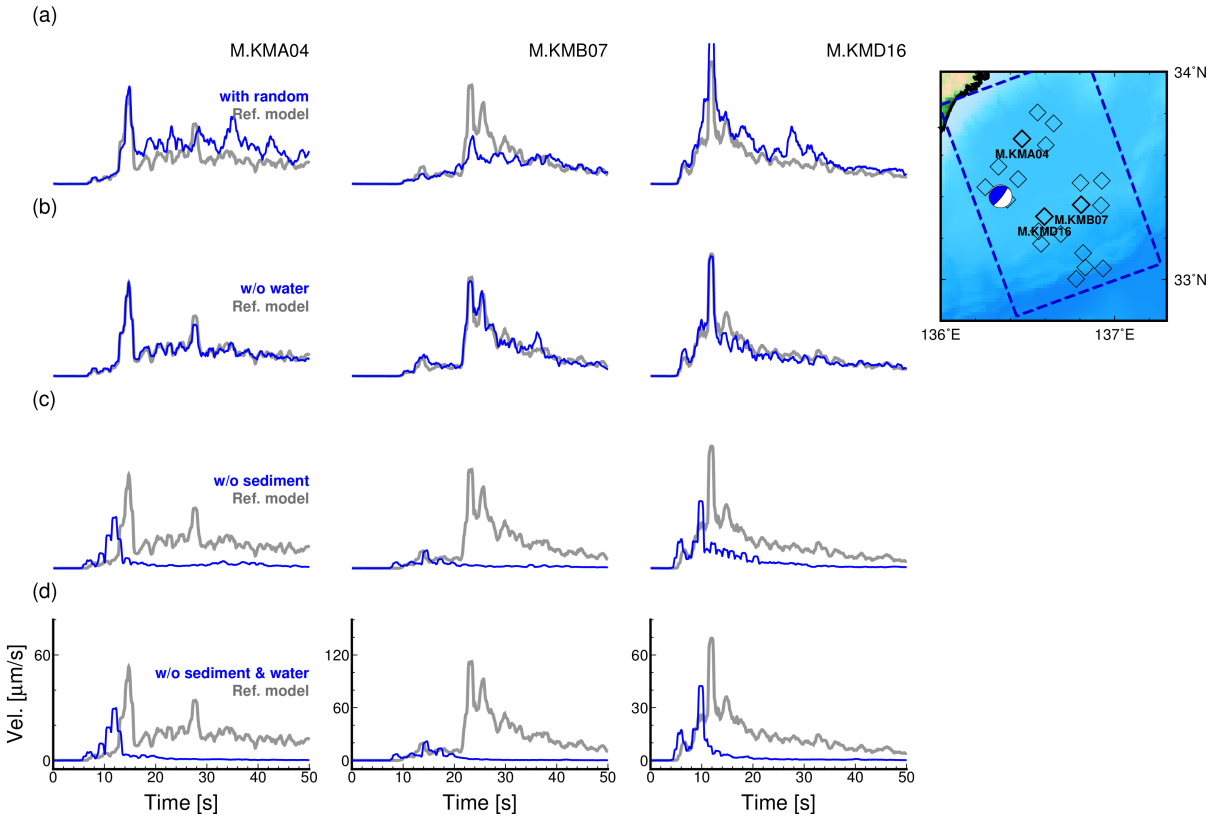

Figure S8. Simulation results of various heterogeneous models for an interplate earthquake. The blue lines are RMS envelopes derived from models: (a) with small-scale random velocity heterogeneities, (b) without seawater, (c) without oceanic sediments (accretionary prism), and (d) without oceanic sediments and seawater. Grey lines are the simulation results with the reference model.

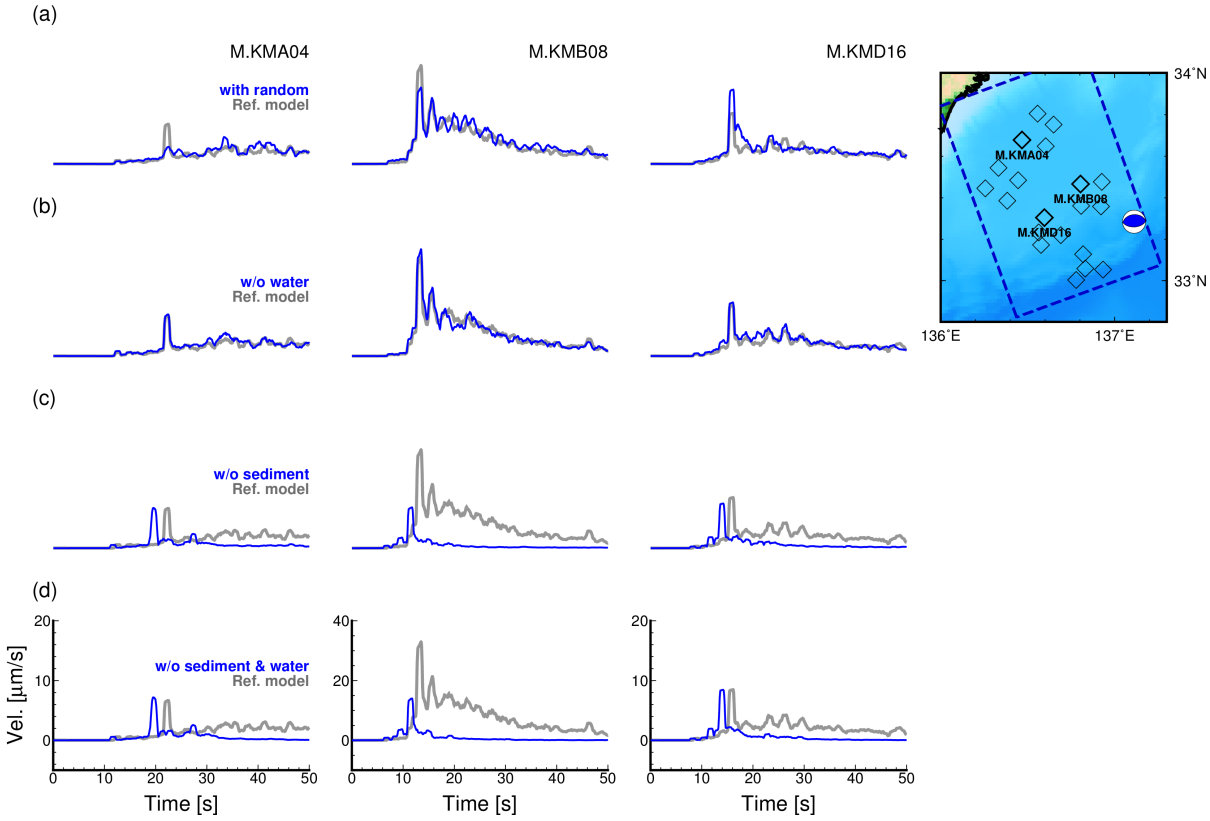

Figure S9. Simulation results of various heterogeneous models for an intraslab earthquake. The blue lines are RMS envelopes derived from models: (a) with small-scale random velocity heterogeneities, (b) without seawater, (c) without oceanic sediments (accretionary prism), and (d) without oceanic sediments and seawater. Grey lines are the simulation results with the reference model.

References

Koketsu, K., Miyake, H., & Suzuki, H. (2012). Japan Integrated Velocity Structure Model Version 1. *Proceedings of the 15th World Conference on Earthquake Engineering*, 1–4. Retrieved from http://www.iitk.ac.in/nicee/wcee/article/WCEE2012_1773.pdf

Maeda, T., Takemura, S., & Furumura, T. (2017). OpenSWPC: an open-source integrated parallel simulation code for modeling seismic wave propagation in 3D heterogeneous viscoelastic media. *Earth, Planets and Space*, *69*(1), 102. https://doi.org/10.1186/s40623-017-0687-2

Takemura, S., Matsuzawa, T., Kimura, T., Tonegawa, T., & Shiomi, K. (2018). Centroid Moment Tensor Inversion of Shallow Very Low Frequency Earthquakes Off the Kii Peninsula, Japan, Using a Three-Dimensional Velocity Structure Model. *Geophysical Research Letters*, *45*(13), 6450–6458. https://doi.org/10.1029/2018GL078455

Takemura, S., Kubo, H., Tonegawa, T., Saito, T., & Shiomi, K. (2019). Modeling of Long-Period Ground Motions in the Nankai Subduction Zone: Model Simulation Using the Accretionary Prism Derived from Oceanfloor Local S-Wave Velocity Structures. *Pure and Applied Geophysics*, *176*(2), 627–647. https://doi.org/10.1007/s00024-018-2013-8

Takemura, S., Matsuzawa, T., Noda, A., Tonegawa, T., Asano, Y., Kimura, T., & Shiomi, K. (2019). Structural Characteristics of the Nankai Trough Shallow Plate Boundary Inferred From Shallow Very Low Frequency Earthquakes. *Geophysical Research Letters*, *46*(8), 4192–4201. https://doi.org/10.1029/2019GL082448

Takemura, S., Okuwaki, R., Kubota, T., Shiomi, K., Kimura, T., & Noda, A. (2020). Centroid moment tensor inversions of offshore earthquakes using a three-dimensional velocity structure model: slip distributions on the plate boundary along the Nankai Trough. *Geophysical Journal International*, *222*(2), 1109–1125. https://doi.org/10.1093/gji/ggaa238

Tonegawa, T., Araki, E., Kimura, T., Nakamura, T., Nakano, M., & Suzuki, K. (2017). Sporadic low-velocity volumes spatially correlate with shallow very low frequency earthquake clusters. *Nature Communications*, *8*(1), 2048. https://doi.org/10.1038/s41467-017-02276-8